

UNIVERSIDADE DE LISBOA
FACULDADE DE CIÊNCIAS
DEPARTAMENTO DE FÍSICA



**Design of a Diffusion Phantom for Quality Control of
Spinal Cord DTI and EPI Distortion Improvement**

Bruno Miguel de Brito Robalo

Mestrado Integrado em Engenharia Biomédica e Biofísica
Perfil em Radiações em Diagnóstico e Terapia

Dissertação orientada por:

Dr. Bailiang Chen, INSERM U947 Imagerie Adaptative Diagnostique et Interventionnelle

Dr. Rita Nunes, Instituto de Biofísica e Engenharia Biomédica, Faculdade de Ciências da

Universidade de Lisboa

2016

If I have seen further it is by standing on the shoulders of giants.

- Sir Isaac Newton

ACKNOWLEDGEMENTS

First of all I want to express my deepest gratitude to all those who provided me the opportunity to carry out this internship and work in an exceptional research team. I am very thankful to INSERM and IADI for accepting me in their team and for funding my internship. I also want to acknowledge the help and dedication of IADI director, Pr. Jacques Felblinger, who promotes a spirit of fellowship, always encouraging the trainees to show and be confident in their work.

To my supervisors Gabriella Hossu and Bailiang Chen, I want to say that I could not have been luckier. Special thanks for your continuous guidance, patience, encouragement, and for always being there when I needed support with work or the French administration. I had the privilege of being supervised by two excellent professionals and I can say that I learned so much and came to appreciate and pursue a career in research. Thank you for everything. During these seven months I also had the privilege to learn from experts in MRI and programming, like Freddy Odile, who was always very helpful and transmitted a great deal of knowledge. I also want to thank my internal supervisor, Pr. Rita Nunes, for always being very helpful and giving valuable inputs for my work.

I am grateful to the entire IADI team for providing the best work environment, especially my office mates Maya, Antoine and Claire for always being so friendly, and for all the joyful times that made work easier. I would also like to express my gratitude to my flatmate and friend Pedro for all the good times, beers and cooking that made my stay in Nancy even more enjoyable.

Thanks to all my friends and colleagues, André, Carlos, Joana, Guimarães and Zé Nuno, with whom explored some parts of Europe. Despite being abroad you made me feel home. My gratitude to a special person, Mariana, for your words of encouragement, patience, friendship and caring heart that always helped through rough times.

Lastly I would not forget my family, the most important people in my life. To my sisters Evelyn and Vania, for your daily support and companionship. To my brother Samuel, for being a role model to me. And finally to my parents José and Maria, for being to the two pillars of my life, for all your support and for always believing in me no matter the circumstances.

RESUMO

A imagem ponderada em difusão (DWI) é uma técnica de ressonância magnética (MR) capaz de medir a magnitude da difusão de moléculas de água nos tecidos. A extensão desta técnica, a imagem por tensor de difusão (DTI) utiliza gradientes aplicados ao longo de pelo menos seis direções diferentes no espaço e deste modo é capaz de estimar também a principal direção de difusão das moléculas de água nos tecidos. Conseqüentemente é possível obter informações sobre a microestrutura de órgãos complexos como o cérebro e a medula espinhal. Estruturas como a substância branca do cérebro e da medula espinhal, que são compostas por microfibras orientadas de forma coerente, são os principais alvos de estudo de DTI, visto que esta técnica é mais sensível a alterações que possam ocorrer na microestrutura de nervos ou neurónios.

Contudo, a medula espinhal é um órgão que apresenta vários desafios em MR, especialmente em DTI. Em primeiro lugar, a medula espinhal tem uma dimensão relativamente pequena quando comparada com outros órgãos e isto impõe dificuldades em termos da razão sinal-ruído (SNR). Para além disso, as diferenças de suscetibilidade magnética entre diferentes tipos de tecidos (medula espinhal, líquido cefalorraquidiano - LCR, osso, etc.) faz com que o campo magnético seja menos homogêneo nessas regiões, o que por sua vez tem influência na origem de artefactos e distorções da imagem. Outras complicações estão relacionadas com movimentos fisiológicos (batimento cardíaco, respiração e fluxo do LCR). Em suma, estas complicações podem resultar em estimativas erróneas dos parâmetros de DTI, o que pode influenciar o diagnóstico.

Com a evolução do *hardware* de MR e o desenvolvimento de novas sequências de impulsos, e a implementação de técnicas de imagem rápidas fez com que o DTI fosse praticável em ambiente clínico. A *echo-planar imaging* (EPI) é a principal sequência utilizada em DTI e permite a obtenção de uma imagem em menos de cem milissegundos. Contudo, a EPI é muito sensível a erros de fase e heterogeneidades do campo magnético que causam erros durante a reconstrução de imagem, fazendo com que a presença de artefactos *ghost*, distorções geométricas e de intensidade sejam frequentes. Deste modo, os passos necessários para a melhoria da qualidade de imagem não podem ser ignorados. Isso pode ser conseguido durante a aquisição, modificando as sequências, com a aplicação de técnicas como *partial Fourier* e *parallel imaging* que reduzem a quantidade de linhas do espaço-k que são preenchidas, e conseqüentemente diminuem a acumulação de erros relacionados com a EPI. Outra alternativa foca-se na melhoria da imagem após a aquisição, através

da aplicação de métodos para correção de distorções e remoção de artefactos. Deste modo, quando as dificuldades do DTI da medula espinhal são ultrapassadas, este torna-se numa ferramenta de grande importância para o estudo de diversas patologias que afetam o sistema nervoso central (CNS), como é o caso da esclerose múltipla (MS).

O principal objetivo deste estudo foi a otimização da sequência *standard* de DTI para a medula espinhal utilizada em ambiente clínico, utilizando uma antena *head-neck-spine* recentemente instalada. Para isso, foi construído um fantoma para simular as propriedades de difusão da água na substância branca da medula espinhal. O fantoma é composto por fibras de acrílico inseridas num tubo de plástico com dimensões semelhantes à medula espinhal. Posteriormente, o tubo foi mergulhado em água de modo a que ocorra perfusão das fibras, sendo assim possível simular algumas propriedades de difusão na medula espinhal.

O fantoma foi mantido na sala de MR a uma temperatura estável e foi submetido a várias sessões de MR com o objetivo de determinar a configuração ideal da antena para a obtenção de imagens da medula espinhal, bem como para a obtenção de imagens de DTI que iriam ser utilizadas no pós-processamento. Problemas como a redução de ruído e minimização de artefactos foram abordados durante a aquisição das imagens e durante o pós-processamento.

No pós-processamento, foi aplicado um método baseado na aquisição de duas imagens com gradiente invertido para correção de distorções provocadas por diferenças de suscetibilidade do campo magnético. Este método utiliza duas imagens de DTI obtidas nas mesmas condições e com os mesmos parâmetros, com a exceção do gradiente de codificação de fase que apresentam polaridades opostas, para calcular o mapa de deslocamento dos pixéis. Neste método, durante o cálculo do mapa de deslocamento (DM) dos pixéis responsável pelas distorções, foram aplicadas algumas inovações, nomeadamente um ajuste a uma curva sigmoide seguida por um ajuste a uma superfície polinomial. O método modificado foi otimizado e comparado com o original em termos de robustez na redução de distorções. Por fim, o mesmo protocolo de imagiologia e métodos de melhoria de qualidade de imagem foram aplicados a imagens de voluntários saudáveis.

Os resultados demonstraram que o fantoma se manteve estável e as imagens obtidas foram reprodutíveis durante o decorrer do estudo. Os parâmetros de DTI como a anisotropia fracionada (FA) e o coeficiente de difusão aparente (ADC) foram calculados várias vezes e o seu valor foi sempre dentro dos limites espectáveis. Para além disso, os mapas de codificação de cores FA mostram que foi conseguida uma difusão anisotrópica nas fibras de acrílico, sendo que a difusão ocorre predominantemente na direção paralela à orientação das fibras tal como acontece no caso

da substância branca da medula espinhal. As imagens de tractografia também mostram que as fibras são claramente distinguíveis das outras estruturas.

Nas imagens de DTI não corrigidas, existem distorções geométricas e de intensidade, sendo que na região das fibras existem curvaturas e erros na estimativa da direção das fibras, fazendo com que a imagem não seja uma representação fidedigna do fantoma físico. Após a aplicação, na sua implementação original, do método de gradiente invertido para a correção de distorções, as regiões com baixa intensidade de sinal continuam a apresentar curvaturas e são mal representadas. Quando são aplicados o ajuste sigmoide e o ajuste à superfície polinomial, o método torna-se mais eficiente, sendo capaz de minimizar as distorções em regiões de baixo sinal, bem como no resto da imagem. Quando o mesmo método é aplicado às imagens de humanos, verifica-se que nas regiões da imagem em que apenas existem distorções e não ocorrem artefactos *ghost*, o método de correção é capaz de minimizar essas distorções. Contudo, na presença de artefactos que não sejam apenas distorções, a correção é menos eficiente.

Em suma, o fantoma apresentado, apesar de ser uma simplificação da estrutura complexa da medula espinhal, é um objeto estável que permitiu o estudo e otimização de uma sequência de DTI para a medula espinhal, bem como o teste de métodos de pós-processamento para a melhoria da qualidade de imagem.

Palavras-chave: Fantoma de difusão, imagem por tensor de difusão, medula espinhal, distorções de suscetibilidade magnética, tractografia, substância branca.

ABSTRACT

Diffusion tensor imaging (DTI) is a magnetic resonance imaging (MRI) technique capable of measuring the magnitude and direction of diffusion of water molecules within tissue and, consequently, give an insight into the microstructure of complex organs such as the brain or the spinal cord.

However, DTI of the spinal cord is arguably one of the most challenging applications of MRI to the human body. Problems such as the small size of the spine, magnetic susceptibility differences between surrounding tissues, local field inhomogeneities and bulk motion can cause image deterioration, artifacts and distortions that ultimately result in erroneous estimations of DTI parameters. With the evolution of coil technology, MR pulse sequences and the employment of fast imaging techniques, DTI is becoming an important tool in clinical settings for the study of pathologies that affect the central nervous system (CNS), such as multiple sclerosis (MS). However, the steps necessary to improve image quality cannot be ignored: during acquisition with methods such as partial Fourier and parallel imaging or after acquisition with post-processing methods.

The main goal of this work was to optimize the standard DTI sequence for the spine using a newly installed coil. First, a diffusion phantom was built to simulate the diffusion properties of white matter in the spine. The phantom is composed by acrylic fibers tightened inside a plastic tube with dimensions similar to those of the spine and then perfused with water. Several scans were performed on the phantom in order to determine the optimal coil configuration as well as to obtain DTI images for post-processing. Here, a distortion correction method based on the reversed gradient correction was applied to minimize susceptibility distortions. The correction method uses two DTI datasets with opposite phase-encoding directions in order to estimate the pixel displacement map (DM) that causes the intensity and geometric distortions. Here, some novelties were applied to the reversed gradient method in the calculation of the DM, namely a sigmoid fit followed by a polynomial surface fit. Finally, the same protocol and processing steps were applied to images from healthy volunteers.

The results show that the phantom was stable and the obtained images displayed a good reproducibility over time. DTI metrics such as FA (fractional anisotropy) and ADC (apparent diffusion coefficient) were within the expected range and the fibers were clearly distinguishable in

color maps and tractography images. The phantom allowed a continuous study and optimization of the distortion correction method.

As expected, when no correction is applied, the DTI images present severe geometric and intensity distortions. When the original reversed gradient correction is applied, regions of the image with low signal, namely the fiber bundles, are still not accurately represented since the noise influences the calculation of the DM. When the sigmoid and surface fit are added to the original method, the distortions in the regions of low signal are minimized. Finally, when the method is applied to human data, regions that are only affected by susceptibility distortions are corrected but in the presence of ghost artifacts and motion, the method is less robust and cannot fully improve the distorted regions.

In summary, the phantom is a simplification of the spinal cord, but nevertheless it is a reliable object that allows the study and optimization of DTI protocols for the spine, as well as processing methods for the improvement of image quality.

Key-words: Diffusion phantom, diffusion tensor imaging, spinal cord, magnetic susceptibility distortion, fiber tractography, white matter.

CONTENTS

ACKNOWLEDGEMENTS	i
RESUMO	ii
ABSTRACT	v
CONTENTS	vii
LIST OF TABLES	ix
LIST OF FIGURES	x
LIST OF ABBREVIATIONS	xiv
INTRODUCTION	1
1 BACKGROUND	3
1.1 Diffusion Tensor Imaging	3
1.2 Echo-Planar Imaging (EPI)	6
1.3 K-space and Parallel Imaging	7
1.4 Partial Fourier	9
1.5 EPI susceptibility distortion	10
1.6 Distortion correction	11
1.7 State-of-the-art of spinal cord DTI	12
2 MATERIALS & METHODS	18
2.1 Phantom Design	18
2.2 Hardware	19
2.2.1 Coil Decoupling	19
2.2.2 Data analysis	21
2.3 Phantom experiments	22
2.3.1 Imaging protocol	22
2.3.2 Reconstruction	23

2.3.3	Distortion correction	23
2.3.4	Data analysis	29
2.4	Healthy volunteer studies	31
3	RESULTS.	32
3.1	Coil decoupling	32
3.2	Distortion correction	35
3.3	DTI metrics	44
3.4	Healthy volunteer studies	46
4	DISCUSSION	48
5	CONCLUSION AND PERSPECTIVES	51
	REFERENCES.	52
	APPENDIX I	57

LIST OF TABLES

Table 2.1 - Coil configurations	20
Table 2.2 - Organization of the data for the Wilcoxon test. Each column is a group and the slice number is the criterion for the paired test.	22
Table 2.3 - Organization of the data for the comparison of mutual information.	30

LIST OF FIGURES

Figure 1.1 - Illustration of Spin Echo Diffusion Weighting Sequence with the 90° and 180° RF pulses and diffusion gradients in gray (top). The middle section represents the effect of the diffusion gradients on the phase of the molecules in the sample. Finally, the bottom section represents the MR signal decay with time. a) - In absence of motion the phase offset introduced by the first gradient is canceled by the second. b) - In the presence of diffusion, the phase offset is not canceled after the second gradient, producing an additional signal loss. Note: Image encoding gradients omitted for simplicity purposes. Adapted from [6].	4
Figure 1.2 - a) Spin Echo DWI sequence with EPI readout. b) Corresponding k space trajectory. Adapted from [2].	7
Figure 1.3 - a) Illustration of a fully sampled k-space and an under-sampled k-space that results in an aliased image. b) Coil configuration and respective direction of acceleration. Note that each coil is more or less sensitive to a specific volume of the object. In parallel imaging each coil acquires an under-sampled k-space that results in an aliased image. After application of SENSE or GRAPPA reconstruction a full FOV image is obtained. Adapted from [12].	9
Figure 1.4 - a) ADC map of a sagittal slice of the cervical spinal cord. b) FA maps on of different levels of the spinal cord. Note the higher intensities on the periphery, corresponding to white mater, while grey matter (center) present lower anisotropy. Adapted from [39].	15
Figure 1.5 - Sagittal T2 MRI image (A) in comparison with DT tractography images acquired in two diagonally opposite planes. Three-dimensional tractography images acquired in the medio-lateral and anterior-posterior (B and C) planes show the disrupted fiber tracts [41].	16
Figure 1.6 - A: MR imaging of a spinal cord involvement due to a solid state astrocytoma. FA map and fiber tracking over b0 image show warped fibers around the tumor [42]. B: Selected axial T2-weighted image (left) of the cervical spinal cord of a MS patient acquired at C3 level (the arrow indicates a hyperintense lesion). MD (center) and FA (right) maps corresponding to the level of the T2 weighted image [57].	17
Figure 2.1 - Left - Bundle of acrylic-fibers tightened with (green) plastic cuffs inside a plastic tube; One euro coin used for scale. Right - Final shape of the phantom; the fiber bundle inside a bottle of water (1.5 liters).	18
Figure 2.2 - A - Head-neck-spine coil. Sections A and B contain 6 groups of elements in the posterior part. Section C corresponds to the face group, section D is the “horseshoe” group and finally section E is the chest group. B - Coil configuration superimposed to a sagittal slice of the head, neck and torso, showing the location of each group relative to the body.	19
Figure 2.3 - Schematic representation of the algorithm used for distortion correction. Only the most relevant steps are show for simplicity purposes.	25

Figure 2.4 - Matlab interface for EPI distortion correction and data analysis. The interface is organized in 4 main panels: “1. Import Data from Archimed”; “2. Reversed Gradient Correction”, “3. Corrected”; “4. Stats”	29
Figure 3.1 - Signal-to-noise ratio in four channels when two coil configurations are used. The red boxplot represents the coil configuration with segments 1-2 and with the chest and face elements. The blue boxplot corresponds to the coil configuration with segments 1-2 and without the face and chest elements. A: Channel 1; B: Channel 2; C: Channel 3; D: Channel 4. The boxplots represent values of SNR in 20 slices. The Wilcoxon test was used for a pairwise comparison between the two coil configurations. The asterisks represent the result of the test, *** ($1.4 \times 10^{-3} \leq p\text{-value} \leq 0.0013$).	32
Figure 3.2 - Signal-to-noise ratio in seven channels for different coil configurations when the chest and face elements are connected. The red boxplot corresponds to segments 1-2, the blue corresponds to 1-2-3 and the green corresponds to 1-2-3-4. The boxplots represent values of SNR in 20 slices. The asterisks mark the result of the Wilcoxon test performed pairwise between the three boxes. Red asterisk over the blue plot is the result between the blue and red boxes; Red asterisk over the green box is the result between the green and the red boxes; Blue asterisk over the green box is the result between the green and blue boxes; * (p-value < 0.05); *** (p-value < 0.001); When no asterisk are present it means that there is no significant difference.	34
Figure 3.3 - Cumulative distribution function. A, B: CDFs of one slice in the I + image before and after sigmoid fit, respectively. Each curve is represents the CDF from one line of the image. Note the smoothness of the curves after the fitting. C: CDF of one line (128) in the I+ image (in red) and in the I- image (in blue) before the sigmoid fit; D: CDF of the same line after sigmoid fit.	35
Figure 3.4 - RMSE between the CDF+ and CDF- before and after sigmoid fit. A: Each point is the RMSE between one CDF+ line and its corresponding CDF- line shown in Figure 3.3. Note that one slice has 256 lines, therefore 256 values of RMSE are calculated. B: Boxplot representation of the values shown in A.	36
Figure 3.5 - A - Preliminary corrected image used to generate a mask; B - Mask; C - Original displacement map calculated from the CDF; D - DM with regions of low signal intensity removed; E - DM fitted to a polynomial surface; F - Final displacement map.	37
Figure 3.6 - Top: A: DTI-EPI dataset with left-right phase encoding direction (blue arrow); B: DTI-EPI dataset with right-left phase encoding direction (blue arrow), the + and - symbolically indicate the PE direction; C: Distortion-free T2 FRFSE image. Bottom: A: Contour (in magenta) of the DTI-EPI+ image superimposed to the T2 FRFSE; B: Contour of the DTI-EPI- image superimposed to the T2 FRFSE; C: Contour of the T2 FRFSE superimposed to the respective image. Red arrows indicate regions distortions.	38
Figure 3.7 - Top: A: DTI-EPI after distortion correction using the original method with no fitting; B: Result after distortion correction using only the sigmoid fit; C: Result after when using both the sigmoid and surface fit in the correction method.	

	Bottom: Contour of the images on the top superimposed to the distortion free T2 FRFSE images. Red arrows indicate regions of low SNR where the correction fails.	39
Figure 3.8	- Mutual information between the DTI-EPI and T2 FRFSE images. A: Boxplot representation of the MI before and after distortion correction with different methods. B-G: Pairwise comparison between the boxplots; The Wilcoxon test was used; the asterisk represent the result of the test, ** ($0.015 \leq p\text{-value} \leq 0.022$). No asterisks are shown when the $p\text{-value} > 0.05$.	40
Figure 3.9	- Fiber tracts computed with the STT technique before distortion correction. Red arrow indicates a curvature in the fiber tracts due to distortion. Red and yellow boxes indicate the regions that were amplified and shown in the bottom images. The left image shows the seed ROI where the fiber tracking begins. The right image shows a region where errors in fiber tracking occur.	41
Figure 3.10	- Fiber tracts computed with the STT technique correction without sigmoid or surface fit. Red arrow indicates a curvature in the fiber tracts due to distortion. Red and yellow boxes indicate the regions that were amplified and shown in the bottom images. The left image shows the seed ROI where the fiber tracking begins. The right image shows a region where errors in fiber tracking occurs.	42
Figure 3.11	- Fiber tracts computed with the STT technique after correction with the sigmoid fit alone. Red arrow indicates a curvature in the fiber tracts due to distortion. Red and yellow boxes indicate the regions that were amplified and shown in the bottom images. The left image shows the seed ROI where the fiber tracking begins. The right image shows a region where errors in fiber tracking occurs.	43
Figure 3.12	- Fiber tracts computed with the STT technique after correction using both the sigmoid and surface fit. The curvature present in figures is minimized. Red and yellow boxes indicate the regions that were amplified and shown in the bottom images. The left image shows the seed ROI where the fiber tracking begins. The right image shows a region where errors in fiber tracking occurred in the previous case.	44
Figure 3.13	- A: FA maps of ten slices. The fiber bundle presents higher values. B: Color coded FA map. The colors are defined by the direction of the main eigenvector and the amplitude is weighted by FA. Note the color code given by the arrow system. Diffusion in the up-down direction is represented in red; Left-right is represented in green, and finally inwards-outwards of the plane is represented by blue. C: ADC maps. Regions containing free water have higher values. D: FA and ADC values in the fiber bundle over a period of 4 months. The Mann-Wallis test shows no significant difference over time; $p\text{-value} > 0.6$.	45
Figure 3.14	- Images from healthy volunteers before correction. Top: A: Dataset with left-right phase encoding direction (blue arrow); B: Dataset with right-left phase encoding direction (blue arrow), the + and - symbolically indicate the PE direction; C: Distortion-free T2 FRFSE image. Bottom: A: Contour (in magenta) of the DTI-EPI + image superimposed to the T2 FRFSE; B: Contour of the DTI-EPI- image superimposed to the T2 FRFSE; C: Contour of the T2 FRFSE superimposed to the respective image. Red arrows indicate distortions. Yellow arrows indicate ghost artifact.	46

Figure 3.15 - Images from healthy volunteers after correction. **Top A:** Post correction using the original method with no fitting; **B:** Result after distortion correction using only the sigmoid fit; **C:** Result after using both the sigmoid and surface fit in the correction method. **Bottom:** Contour of the images on the top superimposed to the distortion free T2 FRFSE images. Red arrows indicate regions where the correction fails. 47

LIST OF ABBREVIATIONS

2D	two-dimensional
ADC	apparent diffusion coefficient
AP	anterior-posterior
CDF	cumulative distribution function
CNS	central nervous system
CSF	cerebrospinal fluid
DM	displacement map
DTI	diffusion tensor imaging
DWI	diffusion weighted imaging
EPI	echo-planar imaging
FA	fractional anisotropy
FE	frequency encoding
FID	free induction decay
FOV	field-of-view
FRFSE	fast recovery fast spin echo
FSPGR	fast spoiled gradient echo
FT	Fourier transform
GM	gray matter
GRAPPA	generalized autocalibrating partially parallel acquisition
HARDI	high angular resolution diffusion imaging
HNS	head-neck-spine
IADI	Imagerie Adaptative Diagnostique et Interventionnelle
MI	mutual information
MR	magnetic resonance
MRI	magnetic resonance imaging
NEX	number of excitations
PE	phase encoding
PGSE	pulsed gradient spin echo

PSF	point spread function
QBI	Q-ball imaging
ReLSEP	Registre Lorraine de la Sclerose en Plaque
RF	radio frequency
rFOV	reduced field of view
SCI	spinal cord injury
SE	spin echo
SENSE	sensitivity encoding
SNR	signal-to-noise ratio
ss-EP	single shot echo-planar imaging
STT	streamline tracking technique
TE	echo time
TR	repetition time
WM	white matter

INTRODUCTION

Diffusion-weighted imaging (DWI) and its extension diffusion tensor imaging (DTI) are magnetic resonance (MR) techniques capable of measuring the magnitude of diffusion of water molecules within tissues. With DTI it is also possible to measure the direction of diffusion, and consequently the estimation of tissue microstructure. Spinal cord DTI is one of the most challenging applications of MR imaging to the human body. Difficulties such as the relative small size of the spine, magnetic susceptibility differences between surrounding tissues (bone, cerebrospinal fluid - CSF, spinal cord), local field inhomogeneities and bulk motion are among the factors that cause image deterioration, artifacts and distortions.

Advancements in software and hardware have allowed for the development of more complex MR pulse sequences, designed specifically to overcome these difficulties. When its inherent imaging challenges are overcome, DTI can be a valuable tool to assess several spinal cord pathologies, which affect both anatomy and physiology, such as multiple sclerosis (MS).

DTI sequences usually employ an echo planar imaging (EPI) readout to avoid macroscopic motion artifacts and reduce the readout time. This can also be coupled with parallel imaging and partial Fourier to further decrease the readout, making DTI feasible in clinical settings. Furthermore, parallel imaging and partial Fourier in EPI reduce the echo train length (ETL) and therefore reduce EPI specific artifacts. However, implementation of parallel imaging in the spinal cord remains challenging, due the geometric arrangement of the coils that is usually in conflict with the preferred phase encoding (PE) direction. These fast imaging capabilities always come with a cost in image quality. EPI is very sensitive to field inhomogeneities that cause image distortion and this is aggravated in the spinal cord. This can be minimized with post-processing algorithms that estimate the distortion field and use it to obtain the undistorted image.

The IADI laboratory where this work was carried out is part of a network that aims to improve knowledge of multiple sclerosis (MS) and to advance research on prevention and treatment. A registry (ReLSEP - *Registre Lorraine de la Sclerose en Plaque*) was opened and since 2009, 180-250 new cases are being included into the registry each year. Several clinical research protocols have been initiated in order to perform MRI on a portion of the network patients, including spinal cord DTI since the spine can also be affected by MS.

In this manuscript, the theoretical background necessary to understand this work is introduced in Chap. 1. Concepts such as DTI, parallel imaging, partial Fourier, EPI and susceptibility distortions are explained (Chap. 1.1 to Chap. 1.6). A state-of-the-art of spinal cord DTI is also disclosed in Chap. 1.7.

The aim of this study was to optimize the standard DTI sequence for the spinal cord using the newly installed head-neck-spine (HNS) coil with a focus on artifact and distortion reduction. For this purpose, a phantom was built to simulate the diffusion properties in the spinal cord (Chap. 2.1). Problems such as field inhomogeneity, noise and artifact reduction were addressed (Chap. 2.3). Optimization of the sequence was performed during acquisition by studying methods such as parallel imaging and partial Fourier (Chap. 2.4.2) and with post processing methods to deal with distortions (Chap 2.4.3). Finally a pilot healthy volunteer study was conducted to ensure the robustness of the implemented optimization steps and to evaluate the reproducibility of the measured DTI parameters (Chap. 2.5).

The results of these studies are presented in Chap. 3 and a discussed in chapter 4. A general conclusion is provided in chapter 5.

1 BACKGROUND

1.1 Diffusion Tensor Imaging

The free induction decay (FID) MR signal can be made sensitive to the movement of water molecules (Brownian motion) within the tissue, providing contrast which reflects their molecular displacement on a sub-voxel scale.

It was however, Stejskal and Tanner that provided a detailed description of a DW MR sequence in 1964 [1]. Briefly, the pulsed gradient spin echo (PGSE) sequence is based on the standard SE sequence with an additional pair of identical diffusion weighting gradients placed symmetrically on both sides of the 180° RF pulse, which makes the sequence sensitive to the diffusion of water molecules. A detailed explanation of MRI and the standard SE sequence is beyond the scope of this work but it can be found in references [2, 3]. As shown in Figure 1.1, the first diffusion gradient, before the 180° pulse, adds an additional phase offset dependent on each molecule's position. After the 180° refocusing pulse, if the molecule's position did not change, the second diffusion gradient will reverse the phase offset. In this case, the only signal loss that will be measured is due to the T2 relaxation process. However, if there is motion due to diffusion in the direction of the applied gradients, the individual positions will differ between the application of the first and second diffusion gradients. Therefore, the second gradient will not cancel the phase offset caused by the first. This will result in an additional loss in amplitude of the signal that is independent of the T2 relaxation.

The degree of signal loss can be quantified by the following equation [1, 4, 5]:

$$S = S_0 \exp(-bD) \tag{1.1}$$

Here, S is the signal intensity, S_0 the signal intensity when no diffusion gradients are applied, b is the diffusion sensitizing factor (b-value) and D the apparent diffusion coefficient (ADC), usually expressed in mm^2/s . The b-value (s/mm^2) carries the information about the diffusion encoding gradients and can be expressed as:

$$b = \gamma^2 G^2 \delta^2 \left(\Delta - \frac{\delta}{3} \right) \tag{1.2}$$

Here, γ is the gyromagnetic ratio of the nucleus, G the gradient amplitude, δ the duration of the gradient and Δ the time interval between the applications of the two gradients.

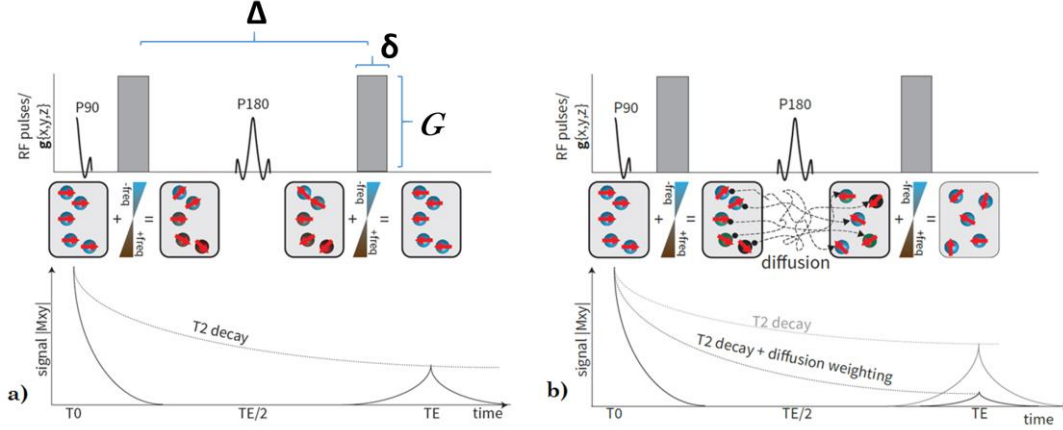


Figure 1.1 - Illustration of Spin Echo Diffusion Weighting Sequence with the 90° and 180° RF pulses and diffusion gradients in gray (**top**). The **middle** section represents the effect of the diffusion gradients on the phase of the molecules in the sample. Finally, the **bottom** section represents the MR signal decay with time. **a)** - In absence of motion the phase offset introduced by the first gradient is cancelled by the second. **b)** - In the presence of diffusion, the phase offset is not cancelled after the second gradient, producing an additional signal loss. Note: Image encoding gradients omitted for simplicity purposes. Adapted from [6].

By performing at least two experiments with different b-values, b_1 and b_2 (usually $b_1 = 0 \text{ smm}^{-2}$), one can extract the ADC of the sample by means of:

$$D = -\frac{1}{b_1 - b_2} \ln \left(\frac{S(b_1)}{S(b_2)} \right) \quad (1.3)$$

Where $S(b_1)$ and $S(b_2)$ represent...

With this sequence, a contrast can already be achieved and ADC maps can be generated.

In pure water, the molecules move randomly without any predominant diffusion direction, therefore there is an isotropic diffusion. In biological tissues, such as gray matter, despite being practically isotropic, diffusion is hindered by macromolecules and cell structures. In white matter of the brain for example, motion of water parallel to axon fibers is facilitated while motion in the perpendicular direction is restricted, leading to an anisotropic diffusion [7].

In order to estimate directionality, the concept of diffusion tensor was introduced by Bassler et al. [8]. Here, Equation (1.1) can be extended to reflect the complete 3-dimensional diffusion covariance matrix, where D is measured in at least 6 directions (in addition to a b_0 image) and fitted by a 3×3 symmetric matrix. The matrix is also positive and definite.

$$D = \begin{bmatrix} D_{xx} & D_{xy} & D_{xz} \\ D_{yx} & D_{yy} & D_{yz} \\ D_{zx} & D_{zy} & D_{zz} \end{bmatrix} \quad (1.4)$$

By diagonalization of the tensor we obtain three eigenvectors e_1 , e_2 , e_3 and their corresponding eigenvalues $\lambda_1 \geq \lambda_2 \geq \lambda_3$. The first eigenvector can be interpreted as the principal diffusion direction and λ_1 its amplitude. This eigenvector is assumed to represent the main direction of the fibers in that voxel [9]. The first eigenvalue is also known as axial diffusivity (parallel to the fibers) while the mean of λ_2 and λ_3 represent radial diffusivity (perpendicular to the fibers).

Given these parameters, other metrics can be computed:

$$ADC = \frac{\lambda_1 + \lambda_2 + \lambda_3}{3} \quad (1.5)$$

The fractional anisotropy (FA) that represents the degree of diffusion anisotropy in each voxel (0, isotropic; 1, anisotropic) is derived as:

$$FA = \sqrt{\frac{3}{2}} \frac{\sqrt{(\lambda_1 - ADC)^2 + (\lambda_2 - ADC)^2 + (\lambda_3 - ADC)^2}}{\sqrt{\lambda_1^2 + \lambda_2^2 + \lambda_3^2}} \quad (1.6)$$

In order to accurately estimate diffusion metrics and fiber orientations, DTI sequences acquiring more than six images corresponding to non-coplanar diffusion directions are required. In this case, the 3×3 tensor matrix is obtained by linear least-square fit as explained in detail by Kingsley [10]. Using matrix algebra, this model can be summarized by the following equation:

$$Y = Hd \quad (1.7)$$

Here, d is the unknown six-element column vector representing the tensor matrix,

$$d = [D_{xx}, D_{yy}, D_{zz}, D_{xy}, D_{xz}, D_{yz}]^T \quad (1.8)$$

H is a large $M \times 6$ matrix, containing the gradient direction coefficients. M is the number of gradient directions and each gradient direction g_i is represented by a vector (G_{xi}, G_{yi}, G_{zi}) ,

$$H = \begin{pmatrix} G_{x1}^2 & G_{y1}^2 & G_{z1}^2 & 2G_{x1}G_{y1} & 2G_{x1}G_{z1} & 2G_{y1}G_{z1} \\ G_{x2}^2 & G_{y2}^2 & G_{z2}^2 & 2G_{x2}G_{y2} & 2G_{x2}G_{z2} & 2G_{y2}G_{z2} \\ \vdots & \vdots & \vdots & \vdots & \vdots & \vdots \\ G_{xM}^2 & G_{yM}^2 & G_{zM}^2 & 2G_{xM}G_{yM} & 2G_{xM}G_{zM} & 2G_{yM}G_{zM} \end{pmatrix} \quad (1.9)$$

Lastly, the left side of Equation (1.7) is defined as:

$$Y = \left(\ln \frac{S_0}{b}, \ln \frac{S_1}{b}, \dots, \ln \frac{S_M}{b} \right)^T \quad (1.10)$$

Note that apart from the signal intensities for each gradient direction (S_i), another measurement with $b = 0 \text{ smm}^{-2}$ is required (S_0). In equation (1.7) the only unknown term is d . For six gradient directions ($M = 6$), the equation has an exact solution. When more than six diffusion gradient direction are used, an approximate solution can be obtained by linear least square fit [10].

1.2 Echo-Planar Imaging (EPI)

In DTI, one measures microscopic motion of water molecules due to diffusion while simultaneously trying to avoid macroscopic motion due to respiration and other physiological mechanisms, meaning that a fast imaging capability is required.

Echo-planar imaging is one of the fastest MR imaging techniques, capable of acquiring an image in less than 100 ms [2, 11]. In conventional imaging, one line of imaging data (one line in k-space or one phase-encoding step) is collected within each repetition time (TR). The pulse sequence is then repeated for multiple TR periods until all phase-encoding steps are collected and k-space is filled. Therefore, the imaging time is equal to the product of the TR and the number of phase-encoding steps. In single shot EPI, multiple lines of imaging data are acquired after a single RF excitation. Like a conventional SE sequence, a SE-EPI sequence begins with 90° and 180° RF pulses. However, after the 180° RF pulse, the frequency-encoding gradient oscillates rapidly from a positive to a negative amplitude, forming an echo train (Figure 1.2 a). Each echo is phase encoded differently by phase-encoding (PE) blips on the PE axis. Each oscillation of the frequency-encoding gradient corresponds to one line of imaging data in k space, and each blip corresponds to a transition from one line to the next in k-space as illustrated in references [2, 12].

With this sequence, acquisition times of 100 ms/slice can be achieved. However, EPI suffers from several artifacts linked to: sensitivity to magnetic susceptibility, which can be reduced by acquiring a shorter echo train (parallel imaging and/or partial Fourier); gradient imperfections (particularly induced currents) which perturb spatial encoding, leading to ghost images [12].

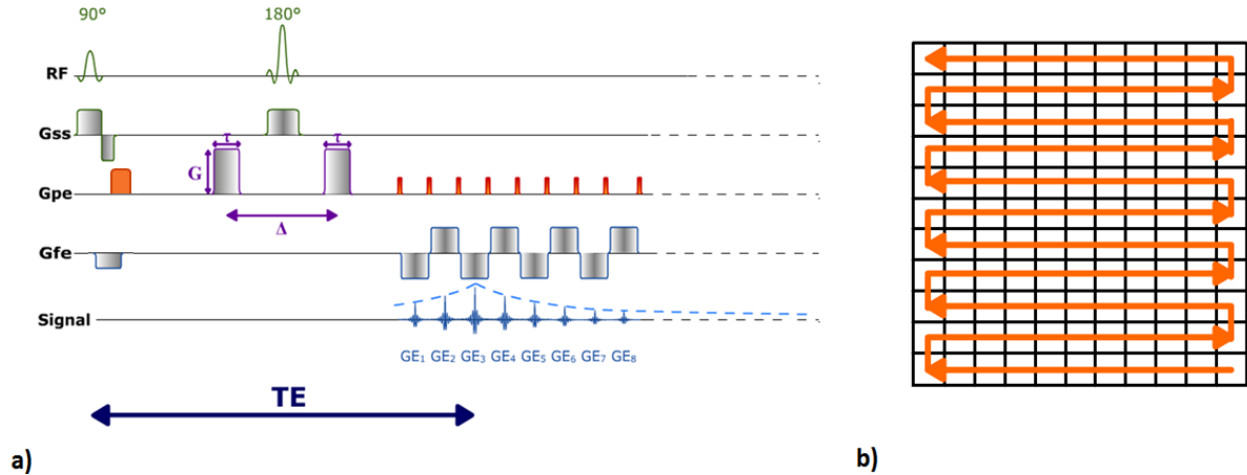


Figure 1.2 - a) Spin Echo DWI sequence with EPI readout. b) Corresponding k space trajectory. Adapted from [2].

1.3 K-space and Parallel Imaging

In MRI, information about the image is collected in k-space which contains spatial frequency information and is related to the actual image through the Fourier transform (FT). The spacing between k-space points is inversely proportional to the field-of-view (FOV) in that direction. For example, decreasing the spacing in y-direction of k-space will result in increase of FOV in the same direction in the image domain. The highest frequency collected in k-space ($k_{x,max}$ or $k_{y,max}$) is inversely proportional to the image resolution, or spacing between points in the image domain (Δx or Δy , respectively). The FOV and resolution can be manipulated by changing the number of points acquired in k-space, the spacing between these points and the k-space spanned by these points [13].

In conventional sequences, k-space data are acquired line by line in order to fill the entire grid of points before the inverse FT is applied to obtain the final image. The k_x direction is the frequency-encoding direction and the k_y direction is the phase-encoding direction. In general, the acquisition time is proportional to the time necessary to read one line (repetition time, TR) multiplied by the number of lines (phase-encoding steps) [13].

One possibility to decrease acquisition time is to reduce the amount of k-space data collected by under-sampling in y-direction, in other words, by increasing the spacing between the lines. In this case the original resolution is maintained because the highest frequencies are also collected but the FOV in y-direction is reduced which will result in aliasing (Figure 1.3 a). The reason for this is that as the k-space data are under-sampled, a high-frequency originating from one part of the object is indistinguishable from a low frequency signal originating from another part of the object and the two locations will overlap in the image (aliasing). The spacing between points in k-space needs to be small enough so that the frequencies from different locations within the object can be distinguished from one another. The FOV should be at least as large as the image size of the object. This is known as the Nyquist criteria [14].

In parallel imaging the acquisition is accelerated by collecting fewer phase-encoding lines in k-space (under-sampling), which will result in aliased images that must be corrected for clinical purposes. There are several parallel imaging methods but they are all based on the same principles [13]:

1. **K-space data are under-sampled in the phase-encoding direction to reduce the scan time.** The acceleration factor R , is inversely proportional to the number of lines acquired. If the fully sampled image is composed by 80 lines in k-space and the acquisition is accelerated by a factor of $R = 2$, the resulting k-space will only be composed of 40 lines.
2. Data are acquired using an array of independent receiver channels instead of using a large homogeneous volume receiver coil. Each channel is more sensitive to the specific volume of tissue nearest to the coil, which means that the channels provide additional spatial information for image reconstruction. It is important that the PE direction (the direction along the acceleration will be performed) is in accordance with the coil configuration. In other words, the coil geometry must be in such manner that distinct channels have different sensitivities in the PE direction (Figure 1.3 b).
3. A special algorithm, which requires the knowledge of individual coil sensitivities, is used to combine the under-sampled data from each of the receiver coils into the unalised reconstructed image with the full FOV.

Note that parallel imaging is not a pulse sequence but instead a reconstruction algorithm that can be used to reconstruct under-sampled data from any type of pulse sequences. These algorithms can be grouped into two categories: algorithms that act on the aliased images of each coil in the image domain (e.g. SENSE - SENSitivity Encoding) [13, 15] and algorithms that act in the under-

sampled k-space and estimate the missing lines of data (e.g. GRAPPA - Generalized Autocalibrating Partially Parallel Acquisitions) [13, 16].

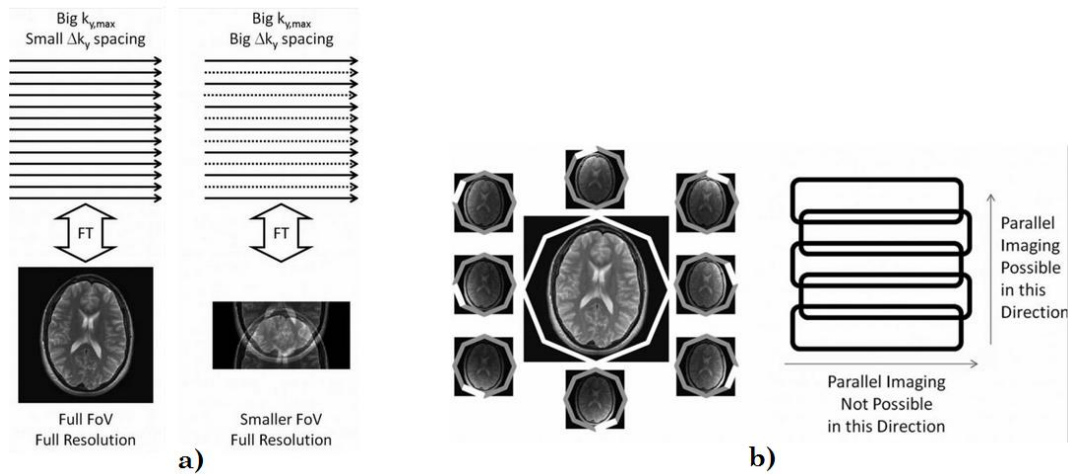


Figure 1.3 - a) Illustration of a fully sampled k-space and an under-sampled k-space that results in an aliased image. **b)** Coil configuration and respective direction of acceleration. Note that each coil is more or less sensitive to a specific volume of the object. In parallel imaging each coil acquires an under-sampled k-space that results in an aliased image. After application of SENSE or GRAPPA reconstruction a full FOV image is obtained. Adapted from [13].

1.4 Partial Fourier

Partial Fourier takes advantage of the conjugate symmetry properties of the Fourier transform. In theory, MRI images represent the spin density as a function of position, hence should be real valued. Since real functions have conjugate symmetry in frequency space (k-space) an image can be reconstructed by acquiring only part of the data (half or more) in the frequency domain. The uncollected data can be synthesized by reflecting conjugate data across the origin of the k-space. Unfortunately there are many sources of phase errors that cause the real-valued assumption to be violated. These include variations in resonance frequency, flow and motion. As a result, partial Fourier reconstruction always requires some type of phase correction that allows a real image to be reconstructed [17].

The simplest method to reconstruct a partial k-space dataset is to simply fill the uncollected data with zeros, followed by inverse 2D FT and display the magnitude. This works well if the fraction of k-space collected is close to 1 and works poorly when this fraction approaches 0.5. The result is significant blurring in the phase-encoding direction. The reason for the blurring can be identified by considering the partial dataset to be a product of the full k-space multiplied by a

weighting function (a step function). In order to correct for the blurring, the missing uncollected data must be synthesized by exploring the k-space symmetry. However, phase correction must not be skipped [17].

Methods such as Homodyne reconstruction and Iterative partial k-space reconstruction apply phase correction and then the conjugate symmetry principle in one or several steps, respectively [17].

1.5 EPI susceptibility distortion

Magnetic susceptibility (χ) is a property of material that characterizes the degree to which the material interacts with the external magnetic field. There is microscopic variation of the magnetic field near the interface between substances with different magnetic susceptibility. In the human brain, large variation of the B_0 field can be observed near the sinuses which are the interface of air and water (brain tissue) as well as in the spinal cord close to bone-CSF interfaces and in regions of the thoracic spine due to the proximity of the lungs. Since the field inhomogeneity is proportional to susceptibility inhomogeneity and field strength, the higher the field strength, the worse the artifacts are [18]:

$$M_{induced} = \chi B_0 \quad (1.11)$$

Two kinds of artifacts can be caused by susceptibility: local signal loss due to dephasing within the voxel (intravoxel dephasing) and geometric image distortion (voxel shift). The MR signal in the presence of field inhomogeneity $\Delta B_0(x, y)$ can be expressed by [18]:

$$s(t) = \iint m(x, y) \exp[-i2\pi(k_x(t)x + k_y(t)y)] \exp[i\gamma \Delta B_0(x, y)t] dx dy \quad (1.12)$$

The second exponential term is the phase error, which is dependent on the field inhomogeneity. According to the time-shift property of the Fourier transform, after the FT, the phase error becomes the pixel shift in the image space. That is how geometric distortion produced in the MR image is related with the existence of field inhomogeneity due to susceptibility differences. The effect of ΔB_0 on the image also depends on the trajectory used to fill the k-space.

For a conventional sequence, after the RF excitation in each TR, one line of k-space is measured. If there is some phase error due to susceptibility difference, it will only occur immediately after the RF excitation and reset to zero after the relaxation (assuming a full relaxation after each TR). Therefore, the phase errors are minimal for the conventional SE sequence. However, the scenario is different for single-shot EPI where the whole k-space is measured (single-shot). The phase error accumulates over the acquisition process. That is the reason that EPI is much more affected by susceptibility distortion. Since the time interval between two lines in the phase-encoding direction is much longer than in the frequency-encoding direction, the geometric distortions is predominantly in the PE direction. Therefore, the phase error in the frequency direction is usually neglected. Equation (1.12) can be written in the form of [18]:

$$s(k_x, k_y) \approx \iint m(x, y) \cdot \exp \left[-i2\pi \{ k_x \cdot x + k_y [y + \gamma \Delta B_0(x, y) \frac{\Delta T}{\Delta k_y}] \} \right] dx dy \quad (1.13)$$

After the Fourier transform, the pixel displacement in the image space can be quantified as:

$$\Delta y = \gamma \Delta B_0(x, y) \Delta T \quad (1.14)$$

Where γ is the gyromagnetic ratio of the nucleus, ΔB_0 is the field inhomogeneity and ΔT the time between successive echoes in the EPI echo train.

1.6 Distortion correction

There are several methods for the improvement of image quality. These algorithms can be categorized into two classes: improvement in the data collecting process and improvement in the post-acquisition process for distortion correction. In the first case the aim is to reduce the phase error accumulation by reducing the amount of k-space lines acquired after each excitation. This can be achieved with parallel imaging. On the other hand, there are post-processing methods that reduce the susceptibility distortions.

The most intuitive and widely used method is field map correction. This method first measures the field inhomogeneity maps and calculates the voxel shift map based on the field inhomogeneity map [19]. However, the field map method requires an additional acquisition to obtain the field inhomogeneity information. It is difficult to accurately match the field map with EPI image pixel-by-pixel. The commonly used smoothing process further limits its accuracy [18]. Furthermore, when the

phase errors overcome a certain limit, phase wrapping will occur, compromising the effectiveness of the method. Another approach is the point spread function (PSF) [20]. In this method, an additional spin-warp PE gradient, which encodes the same spatial information as the EPI PE gradient, is added to the original EPI sequence. After 3D inverse fast Fourier transformation, the reconstructed PSFs are represented along the correlation (or diagonal) line in the spin-warp (or non-distorted) and EPI (or distorted) PE coordinates. Any distortion in the image is reflected in a deviation of the PSFs from the diagonal line along the EPI PE coordinates versus the spin-warp PE coordinates, and thus this deviation of the PSFs allows the accurate calculation of distortions. This method has the potential to provide robust solutions to the distortion problem in regions of high or low field inhomogeneity and allow the correction of both geometric and intensity distortions. However, it is not only more computationally expensive but also has longer acquisition time ($\#PE \text{ lines} \times EPI \text{ acquisition time}$).

Another approach is the reversed gradient method [21, 22] that estimates the distortion field from two EPI images with opposite PE direction and uses it to calculate the undistorted image. The method is described in detail in the Materials & Methods section.

1.7 State-of-the-art of spinal cord DTI

DTI itself is well established and has its main applications in the brain, but much less so in the spinal cord. This part of the central nervous system is a more challenging structure to study. In clinical *in vivo* settings, where acquisition time should be kept as short as possible, these difficulties increase along with the demands on hardware and software performance.

Technical challenges

The small size of the spine and surrounding structures require smaller voxel sizes (higher matrices) for adequate spatial resolution, which will decrease the SNR [23]. The spinal cord is a relatively small structure with approximately 45 cm in length in the adult male, with the largest cross-sectional area in the lower cervical (38 mm circumference) and lumbar regions (35 mm). This means that a sagittal acquisition is usually necessary to obtain sufficient coverage in a reasonable scan time [7]. Nonetheless, axial slices can also be obtained.

Some spinal regions present even greater challenges arising from magnetic susceptibility artifacts due to surrounding bony structures, such as at the cervicothoracic junction, for example.

This results in off-resonance-related artifacts and limits the usable readout duration [24]. Moreover, the bone-CSF and air-bone interfaces in the thoracic region, given the proximity of the pulmonary parenchyma, lead to local field inhomogeneity due to susceptibility differences between tissues, which in turn creates off-resonance induced artifacts in the images. Generally this results in geometric distortions. Furthermore, when moving to higher magnetic fields, these challenges are aggravated as the absolute size of the field perturbations increase with B_0 . The naturally very-curved shape of the spine can also create field distortions [24].

Another problem arises from physiological motion, from cardiac and respiratory cycles, as well as CSF pulsation that results in nonlinear phase errors and shifts/dispersions of k-space when these motions occur during the diffusion encoding gradients and the phase encoding direction is anterior-posterior (AP), resulting in ghosting artifacts and erroneous estimations of DTI metrics [25, 26]. Some of these problems can be reduced by cardiac and/or respiratory gating but the pulsatile motion of CSF remains difficult to overcome and can lead to significant artifacts since they occur independently. With improvement of software and hardware technology, some of these challenges can be minimized, as described below.

Imaging protocols

A fast imaging capability is crucial in order to avoid the effects of macroscopic motion (e.g. respiration). EPI based sequences put enormous demands on hardware capabilities. The requirements for gradient strength, rise time and duty cycle are markedly increased because all of k-space is traversed following a single RF excitation by using a rapidly oscillating frequency-encoding gradient. Modern clinical scanners are usually equipped with gradient strengths of 40 - 70 mT/s and slew rates of 200 T/m/s. In EPI, the full capabilities of the gradients are made use of [12].

The most commonly used technique for DTI is the SE single-shot EPI (ss-EPI). As all data is acquired within a single shot, with this method magnitude images do not suffer from ghosting artifact and higher resolutions can be obtained by acquiring a longer echo train, or by using a multi-shot method. However, image distortions may still persist in regions of inhomogeneous magnetic susceptibility. Distortions can be reduced using parallel imaging in such EPI sequences because the readout duration is reduced, avoiding cumulative EPI errors. Successful implementation and application of parallel imaging in the spine is limited primarily because of the geometric arrangements of spine array coils, which is often in conflict with the preferred anterior-posterior

direction of phase encoding for spine imaging [25]. This direction is preferred over the left-right direction to avoid aliasing of the shoulders and other structures.

Another method that can be used is the reduced field of view (rFOV) ss-EPI technique with imaging performed in the sagittal plane. By reducing the FOV (the RF pulses excite a narrower volume), fewer phase-encoding steps are needed, which, in turn, leads to a more rapid traversal from one end of the k-space to the other. Such technique is better suited to the long and narrow anatomy of the spine and the small cross-sectional size. This method reduces off-resonance-induced artifacts while allowing the use of a ss-EPI method. Previous studies have shown that this method is feasible to use in clinical populations and it is sometimes preferred over the traditional ss-EPI as it provides higher resolution for the same readout time. However, it has lower SNR, the FOV is smaller and some aliasing can occur, but reduces partial volume artifacts [25, 26, 27, 28].

Another interesting option is multi-segment EPI that relies on phase-navigated multi-shot spin echo interleaved technique, which acquires the k-space over multiple shots. The method allows for increased velocity transversal of k-space (PE direction) which reduces EPI-specific artifacts when compared to the standard ss-EPI method. However the acquisition time is greater [25].

Animal studies

Experimental DTI of the spinal cord using animal models, namely rats and mice, are important to test the usefulness of DTI to delineate neural structures in the spinal cord. In these cases, studies must be performed using high-field magnets (> 4.7 T) to provide enough resolution to cope with the small size of the rat/mice spinal cord.

DTI studies on animal spinal cords indicate that DTI metrics clearly differentiate white (WM) and gray matter (GM). Higher anisotropy is characteristic of WM since it is composed by organized fibers [29, 30]. Moreover, significant differences between spinal cord levels (cervical, thoracic, lumbar) in ADC and FA have been described [31]. Anatomical and physiological functions differ along the extension of the spinal cord and DTI proves to be a useful tool to assess its neural microstructure.

Another interesting application of DTI on animal models is the study of the evolution of spinal cord injury. Ford et al. [32] described significant decreases in λ_1 and increases in λ_2 and λ_3 at the level of injury as well as in areas of the cord that were apparently normal on conventional T2-

w images. DTI has also demonstrated the ability to detect changes in diffusion metrics at regions remote from the lesion area [33].

Human studies

Baseline DTI studies in healthy subjects have allowed for the differentiation between WM and GM along the spinal cord, as well as quantitative values of diffusivity and anisotropy. Studies such as the ones performed by Clark et al. [34] and Ries et al. [35] mark baseline quantitative values of ADC for the spinal cord. More recent studies [39] have also shown a clear contrast between GM and WM in the spinal cord when axial slices are acquired (Figure 1.4). WM in the periphery presents higher anisotropy, with FA values around $0.50-0.70 \pm 0.05$. The apparent diffusion coefficient along the extension of the cord averages $0.83 \pm 0.06 \times 10^{-3} \text{ mm}^2/\text{s}$.

Extensions of DTI, high angular resolution diffusion imaging (HARDI) [36] and Q-Ball imaging (QBI) [37], can represent more than one diffusion direction in each voxel and therefore be able to assess the spinal cord in even greater detail, as demonstrated by Cohen-Adad and colleagues [38].

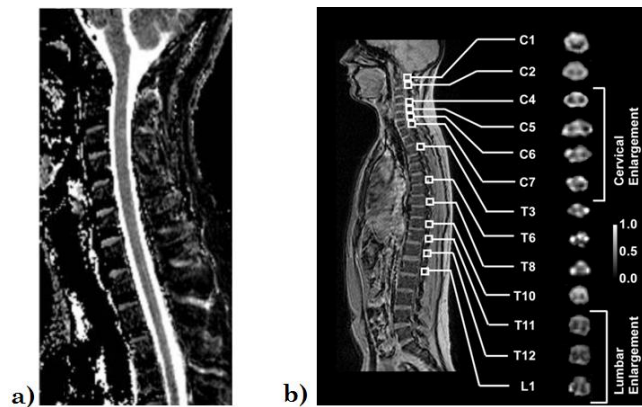


Figure 1.4 - a) ADC map of a sagittal slice of the cervical spinal cord. **b)** FA maps on different levels of the spinal cord. Note the higher intensities on the periphery, corresponding to white matter, while grey matter (center) presents lower anisotropy. Adapted from [39].

Given its sensitivity to fiber organization and directionality, DTI appears to be the ideal imaging technique to study diseases affecting WM structures in the CNS, namely the spinal cord, *in vivo*.

In acute spinal cord injury (SCI), neural injury is characterized by axonal deterioration, and loss of myelin. Therefore, the decrease in FA that is observed is related not only to axonal loss,

meaning that diffusion will no longer occur parallel to the fibers, but it is also related to the augmentation of extracellular space since loss of myelin permits diffusion perpendicular to the fibers (increase of radial diffusivity), hence decrease of anisotropy. Rajasekaran et al. [40, 41] showed that in Brown Sequard syndrome, which in anatomical MRI is merely viewed as a change of intensity at the injury site, when assessed with DTI, the lesions are in fact extended to the spinal cord tracts (Figure 1.5).

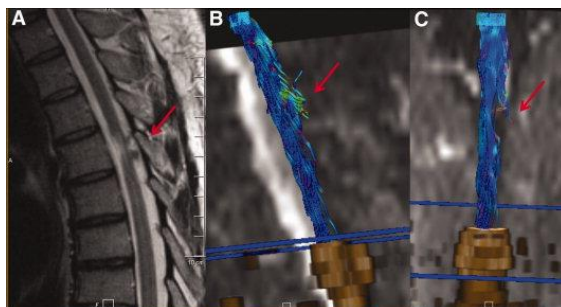


Figure 1.5 - Sagittal T2 MRI image (A) in comparison with DT tractography images acquired in two diagonally opposite planes. Three-dimensional tractography images acquired in the medio-lateral and anterior-posterior (B and C) planes show the disrupted fiber tracts [41].

Neoplasms such as spinal cord astrocytoma can also be assessed with DTI, as shown by Ducreux et al. [42]. This rare pathology can result in alteration of the spinal cord structural integrity and DTI based tractography can reveal detailed information. In this study, in addition to the 2D FA color maps that revealed a decreased anisotropy (FA = 0.48 when compared to 0.78 for healthy subjects), 3D white matter fiber tracts were created. Here, at the site of the tumor it is possible to visualize the warped WM tracts in the solid state astrocytomas (Figure 1.6 A).

MS is a chronic autoimmune disease of the CNS in which the spinal cord is often involved. The pathologic hallmark of the disease is the inflammatory demyelination, which leads to irreversible tissue loss or partial demyelination in cases where reparative processes occur with subsequent remyelination [43]. In anatomical imaging, MS is identified as hyper-intensities. In DTI, MS has been characterized by an increase of the diffusion coefficient and loss of anisotropy (Figure 1.6 B). A decrease of axial diffusivity may be the consequence of axonal loss, whereas an increase of radial diffusivity has been associated with an attempt made by a compensative mechanism to maintain functionality in the presence of WM damage [44, 45].

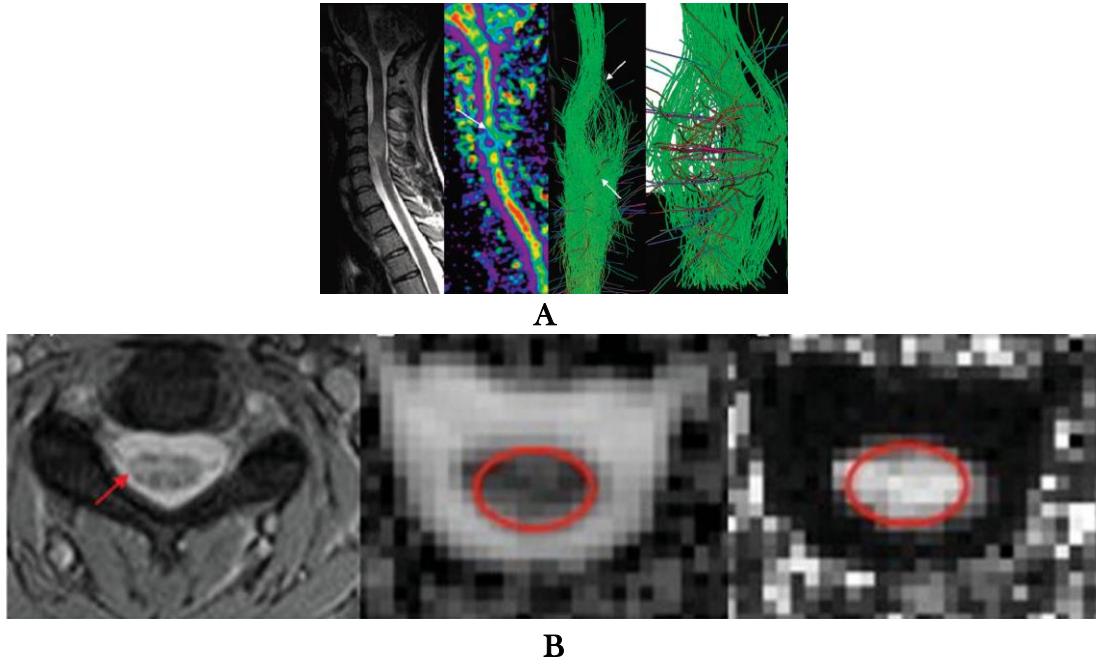


Figure 1.6 - A: MR imaging of a spinal cord involvement due to a solid state astrocytoma. FA map and fiber tracking over b_0 image show warped fibers around the tumor [42]. **B:** Selected axial T2-weighted image (**left**) of the cervical spinal cord of a MS patient acquired at C3 level (the arrow indicates a hyperintense lesion). MD (**center**) and FA (**right**) maps corresponding to the level of the T2 weighted image [57].

In conclusion, DTI gives a unique insight into the microstructure of tissues and allows for more detailed non-invasive studies of pathologies involving the spinal cord such as MS, SCI and tumors.

However, DTI of the human spinal cord still presents a number of limitations. Despite the generalized use of 3 T scanners in clinical settings, achieving adequate spatial resolution and SNR remains a great challenge when imaging such small structures. The implementation of faster imaging techniques such as parallel imaging, compress sensing [47] and EPI, as well as the use of cardiac gating cannot fully compensate for the artifacts and image distortions inherent to DTI. Post-processing steps to correct for artifacts and distortion cannot be ignored.

Studies with phantoms such as the one described in this work are always useful for the optimization of DTI protocols and the study of post processing methods for image quality improvement.

2 MATERIALS & METHODS

2.1 Phantom Design

An artificial phantom was built to simulate the diffusion of water in the spinal cord (Figure 2.1). The phantom was built with common materials that can be found in retail stores. It is comprised of a bundle of artificial fibers tightened together in order to achieve a great density of fibers inside a plastic tube with 1.2 cm in diameter and 22 cm in length. Each single fiber is a composite of acrylic-polyester, similar to synthetic hair, and has a diameter of approximately 100 μm . The bundle was tightened with plastic cuffs and secured inside a bottle of water in order for the water to perfuse the fibers. Here, the anisotropic diffusion will be created by the water molecules that are diffusing in-between the fibers (the “extracellular space”). Care was taken in order to minimize the presence of air bubbles inside the fiber bundles. The phantom was kept in the MRI room during the course of this work.

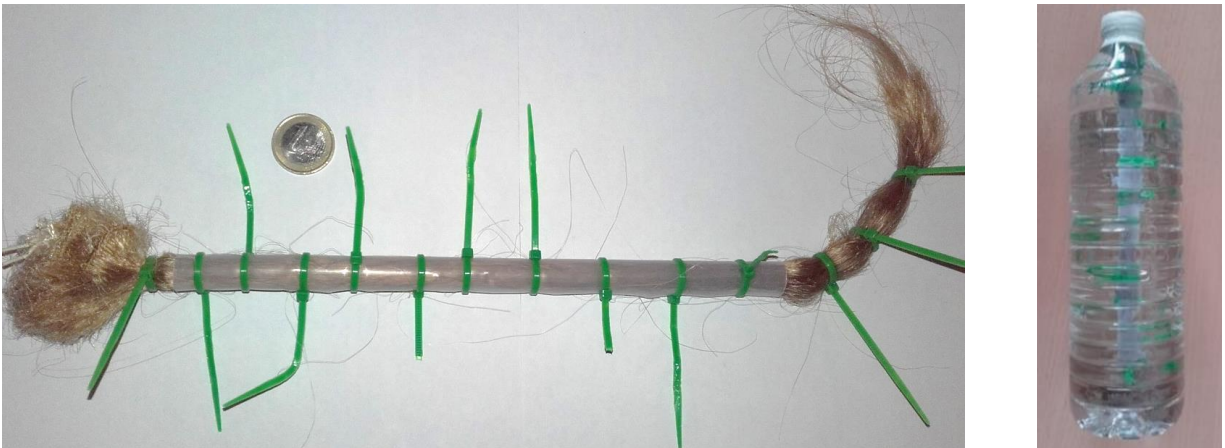


Figure 2.1 - **Left** - Bundle of acrylic-fibers tightened with (green) plastic cuffs inside a plastic tube; One euro coin used for scale. **Right** - Final shape of the phantom; the fiber bundle inside a bottle of water (1.5 liters).

2.2 Hardware

The laboratory is equipped with two General Electrics MR systems. In this work, imaging was performed with a 3 T GE Signa HDxt (GE Medical Systems, Milwaukee, WI, USA) equipped with gradients capable of achieving a maximum amplitude of 85 mT/m and a slew rate of 150 T/m/s. A 16-channel head-neck-spine (HNS) coil that covers the entire brain and spinal cord was used as receiver. A more detailed description of the coil is presented in the following section.

2.2.1 Coil Decoupling

The HNS coil has a total of 29 elements organized in several segments: 6 groups in the posterior part, a face group, a chest group and a posterior head group, in addition to the “horseshoe” group that can be used instead of the face group when one is only interested in the posterior section of the brain and the spinal cord. It is worth mentioning that all the groups cannot all be used at the same time. The maximum number of groups that can be used at any given time is four (1-2-3-4) coupled to the face and chest groups.

These groups correspond to 16 channels. Channels are independent, complete electronic chains required for processing information received from a coil element. The channels include amplifiers, filters, analog-to-digital conversion circuitry, demodulation/mixer devices, and image processing capability. The output of each channel is generally a partial view of the entire anatomy being imaged, subsequently combined with output from the other channels to produce the final MR image [48].

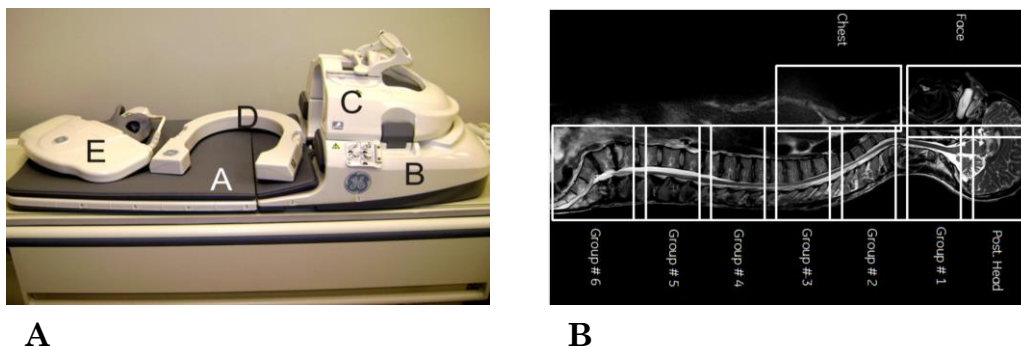
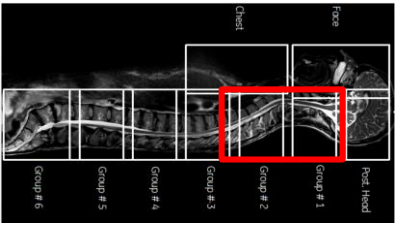
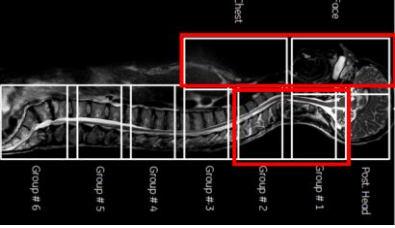


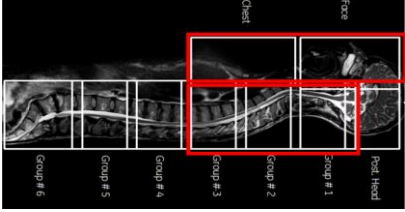
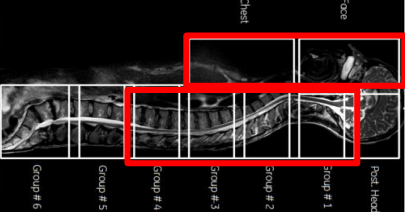
Figure 2.2 - A - Head-neck-spine coil. Sections A and B contain 6 groups of elements in the posterior part. Section C corresponds to the face group, section D is the “horseshoe” group and finally section E is the chest group. **B -** Coil configuration superimposed to a sagittal slice of the head, neck and torso, showing the location of each group relative to the body.

In this work, a coil decoupling experiment was performed in order to test the decoupling circuit between the elements of this coil. In MRI, when using RF coils with multiple elements with different sensitivity distributions, it is important to ensure minimal electromagnetic coupling between these elements so as to avoid interference and/or induction between them [49]. To minimize coupling between elements, optimal coil overlap between nearest-neighbor elements is sought. Furthermore, each coil can have a decoupling circuit with low input impedance preamplifiers to isolate the relatively weak coupling between non-nearest neighbors. Techniques such as the use of capacitor or inductors between two elements can also be employed to reduce coupling [50].

In this study the object of interest (the diffusion phantom) was placed in the section of the coil covered only by groups 1 and 2. The rest of the coil was filled with standard GE water phantoms to simulate the rest of the body and contribute to the noise. Then, in the scanner console, several coil configurations were selected for imaging as described in Table 2.1.

Table 2.1 - Coil configurations

Phantom location	Coil configuration (groups) used	Coil configuration (groups) used
1-2	1-2	 <p>The image shows a sagittal MRI scan of a spine. The scan is divided into six vertical sections labeled 'Group # 1' through 'Group # 6' from right to left. A red rectangular box highlights the area covered by Group # 1 and Group # 2. Labels 'Chest' and 'Face' are visible at the top of the scan, and 'Post. Head' is at the bottom right.</p>
1-2	1-2, face and chest	 <p>The image shows a sagittal MRI scan of a spine, similar to the one above. A red rectangular box highlights the area covered by Group # 1 and Group # 2. A second red rectangular box highlights the 'Face' and 'Chest' regions at the top of the scan. Labels 'Chest', 'Face', and 'Post. Head' are visible at the top and bottom right. The group labels 'Group # 1' through 'Group # 6' are at the bottom.</p>

1-2	1-2-3, face and chest	 <p>The diagram shows a sagittal view of a human torso with six MRI coil groups labeled Group #1 to Group #6. Two red rectangular boxes highlight regions of interest: one for the 'Face' region (top right) and one for the 'Chest' region (middle right). The labels 'Face' and 'Chest' are placed above their respective boxes.</p>
1-2	1-2-3-4, face and chest	 <p>The diagram is identical to the one above, showing six MRI coil groups and two red boxes for 'Face' and 'Chest' regions of interest.</p>

2.2.2 Data analysis

A T1 FSPGR (fast spoiled gradient echo) sequence [51] was used. Signal (with RF excitation) and noise-only (without RF excitation) acquisitions were obtained. The k-space data from each channel was reconstructed separately and the SNR was calculated by dividing the mean signal by the standard deviation of the noise: $SNR = \frac{Signal (mean)}{noise(stdev)}$. For each coil configuration, the SNR in channels 1 to 7 was studied. For each channel SNR was calculated in all slices in Matlab and the data was organized as in Table 2.2. Using R (R Foundation for Statistical Computing, Vienna, Austria) the paired Wilcoxon test was performed between the coil configurations. Here the comparison of SNR is not done directly between different channels but within the same channel when different coil configurations are used (i.e., when other channels are also connected). For example, Table 2.1 is only representing the SNR calculated in channel 1 with different coil configurations. Here, the goal is to test differences indicative of coil coupling, i.e., the following question is posed: is one channel influencing the SNR in another channel.

For all the statistical tests in this work, p-values smaller than 0.05 were considered significant.

Table 2.2 - Organization of the data for the Wilcoxon test. Each column is a group and the slice number is the criterion for the paired test.

<i>Slice</i>	Configuration			
	1-2	1-2, face, chest	1-2-3, face, chest	1-2-3-4, face, chest
<i>1</i>	SNR	SNR	SNR	SNR
<i>2</i>	SNR	SNR	SNR	SNR
<i>3</i>	SNR	SNR	SNR	SNR
<i>:</i>	SNR	SNR	SNR	SNR

2.3 Phantom experiments

2.3.1 Imaging protocol

The imaging protocol was chosen and optimized based on existing clinical protocols used for the ReLSEP registry. For DTI, a PGSE DWI sequence with ss-EPI readout was used. Imaging parameters were optimized as follows: In order to keep the acquisition time under 10 minutes, 15 diffusion gradient with $b = 1000 \text{ s/mm}^2$ were used; an additional non-diffusion-weighted image ($b = 0 \text{ s/mm}^2$); axial slices (slice thickness, 2.0 mm and spacing between slices, 0.2 mm, PE direction anterior-posterior), sagittal slices (slice thickness, 2.0 mm and spacing between slices, 0.2 mm, PE direction anterior-posterior), acquisition matrix of 80×80 and $240 \times 240 \text{ mm}^2$ FOV; TR/TE = 6000/86.7 ms; number of excitations (NEX) = 4; The number of slices used was such that a sufficient coverage of the fibre regions is obtained. In the axial plane, 20-40 slices; in the sagittal plane, 7-14 slices were used. An interleaved slice order was used, with the odd slices being acquired before the even slices. Parallel imaging with an acceleration factor of $R = 2$ was used. Groups 1-2, face and chest were used as the coil configuration. Partial Fourier factor of 0.7. Total acquisition time was approximately 8 minutes.

A second DTI dataset with the same imaging parameters was, with exception for the PE direction was obtained. Here the PE direction was flipped by 180° (posterior-anterior instead of anterior-posterior) by changing a control variable in the scanner console. The acquisition time was approximately 45 seconds, which adds a minimal time to the total acquisition time. Only the b_0 acquisition was obtained.

For comparison purposes, anatomical dataset was obtained. A T2 FRFSE (fast recovery fast spin echo) sequence with the same geometry as the DTI images was used. Other imaging parameters were as follows: acquisition matrix 352×256 , TR/TE = 1509/117 ms.

2.3.2 Reconstruction

The prescribed k-space for the DTI images was an 80×80 matrix but due to acceleration factor of $R = 2$ and partial Fourier acquisition, only 36 phase encoding steps were collected, in order to decrease the readout time and avoid EPI specific artifacts. The raw data obtained from the scanner was an 80×36 k-space with phase shifts between the echoes (odd and even) due to the EPI readout. The odd and even lines of k-space are acquired with opposite polarity, and experimental imperfections such as gradient eddy currents, imperfect pulse sequence timing, B_0 field inhomogeneity and susceptibility differences result in the even and odd lines of k-space being offset by different amounts relative to the true center of the acquisition window [51].

Image processing was performed on the raw data and consisted of phase correction (by multiplication of the k-space with EPI phase correction coefficients provided by the scanner), and reorganization of the lines of k-space by redistributing them in full 80×80 empty matrix, with spacing between the lines in accordance with the acceleration factor used. Note that due to partial Fourier acquisition, the entire span of k-space is not covered. Therefore, apart from SENSE reconstruction to synthesize the missing information in-between the lines, Homodyne reconstruction was also performed to fill the rest of the data. After inverse FT, magnitude images for each slice and each diffusion direction were obtained.

2.3.3 Distortion correction

When the single shot EPI readout is used, regions of field inhomogeneity suffer from severe geometric and intensity distortions. In this work a method based on the reversed gradient correction [21, 22] was developed for distortion correction. Two DTI-EPI datasets with opposite phase encoding directions are necessary. Here, it is assumed that the diffusion gradients do not contribute for the distortions and therefore the second DTI-EPI dataset need not contain all the diffusion directions, only the b_0 acquisition. Note that for a full DTI dataset with 15 directions, the

acquisition time is approximately 8 minutes but when only the b0 image is obtained, the acquisition time is less than 50 seconds.

The algorithm was developed in Matlab R2013a (Mathworks, Natick, MA) and it is summarized in Figure 2.3. Each step is explained in detail below:

1. The first step is to acquire two EPI-DTI images with opposite PE polarities. Here, for better comprehension, the image with the forward PE direction will be called EPI+ or I+ and the image with the reversed PE direction will be called EPI- or I-. Furthermore, because only the distortions in the PE direction (y coordinate) are considered relevant and to simplify the notation, only the y is specified. In these two distorted images, each pixel is displaced from its original position y by Δy , but in opposite directions:

$$y_+ = y + \Delta y \text{ and } y_- = y - \Delta y \quad (2.1)$$

Let us not forget that these two variables are functions of y and should be written $y_+(y)$ and $y_-(y)$ but for simplicity purposes (y) is dropped in some cases. Here, Δy is proportional to the field inhomogeneity. Equation (2.1) simply gives the geometric transformation from the true position y to the distorted positions y_+ and y_- . These two images are representations of the same object.

2. The image integral from 0 to y is the cumulative distribution function (CDF) given by:

$$C(y) = \int_0^y I(Y)dY \quad (2.2)$$

Here, the cumulative distribution function (CDF) is calculated along the PE direction, line-by-line. Considering one line with N pixels, for pixel P, the corresponding CDF is the summation of all the pixels from 1 to P. The process is repeated for all the lines in both images.

3. If the effects of noise and other artifacts apart from distortions are neglected, then both CDF curves should present the same shape and the value for the two points y_+ and y_- should be equal. The calculated CDFs are fitted to a sigmoid function, giving a more smooth shape to the curve. This removes small discrepancies between the shapes of the two curves. By using the least-square method, the parameters (a , b , c and d) that best fit the following equation are estimated.

$$f(x) = \frac{b-a}{1+e^{(c-x)d}} \quad (2.4)$$

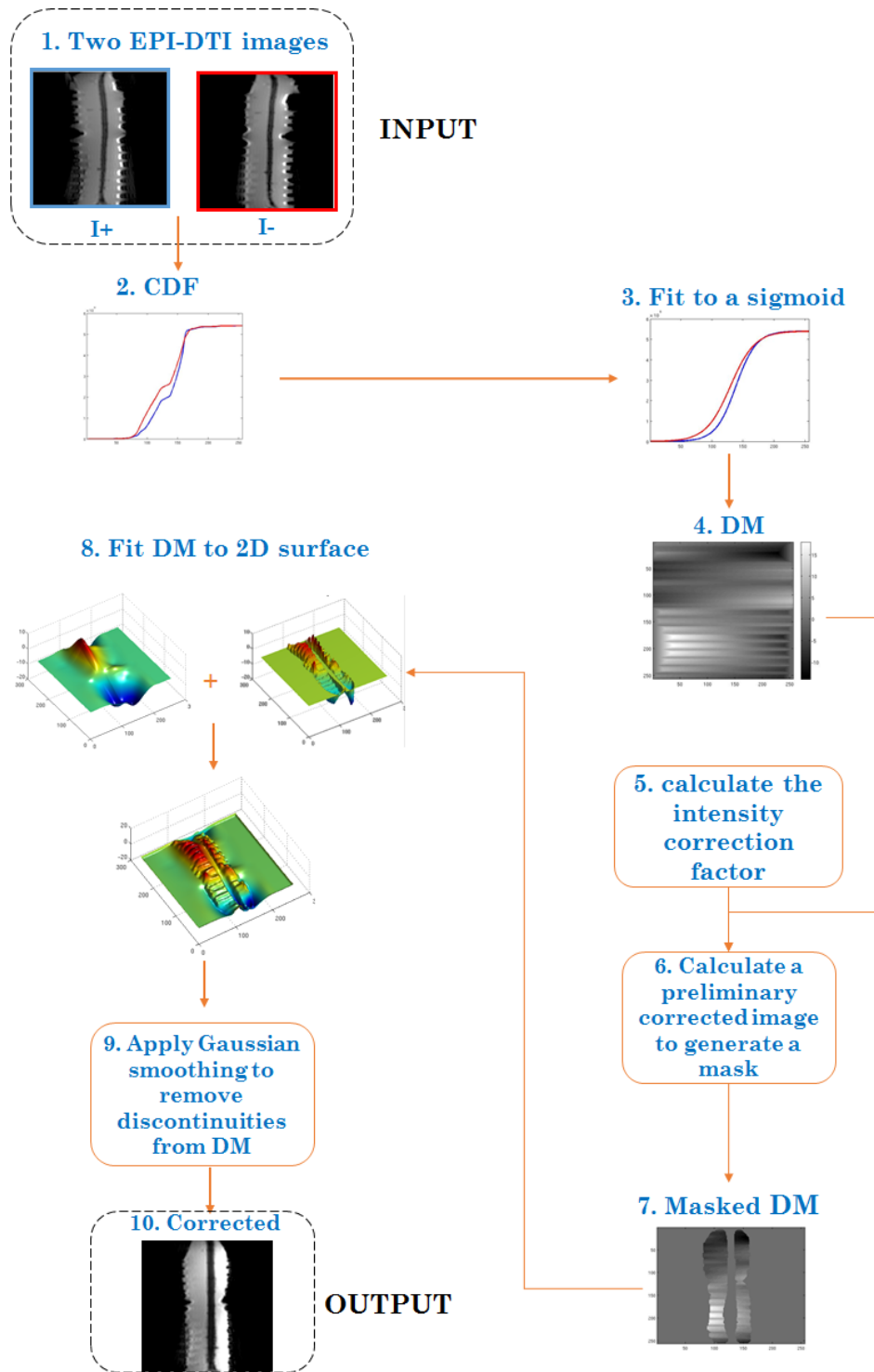


Figure 2.3 -. Schematic representation of the algorithm used for distortion correction. Only the most relevant steps are shown for simplicity purposes. **Step 1**: Acquisition of two EPI images with opposite PE direction; **Step 2**: Calculation of the cumulative distribution function (CDF) of each image; **Step 3** - The CDFs are fitted to a sigmoid function; **Step 4**: Calculation of the displacement map (DM); **Step 5**: Calculation of the intensity correction factor; **Step 6**: Calculation of a preliminary corrected image to generate a mask; **Step 7**: The DM is masked and regions of low intensity are removed; **Step 8**: The DM is fitted to a polynomial surface; **Step 9**: Smoothing; **Step 10**: Calculation of the corrected image.

4. Next, in each line, y_+ and y_- can be recovered as the points that have equal CDF by a search algorithm.

$$C_+(y_+) = C_-(y_-) \quad (2.5)$$

From equation (2.1) the real position y of each pixel in the undistorted image can be found as:

$$y = (y_+ + y_-)/2 \quad (2.6)$$

Now the pixel displacement map (DM) can be obtained by

$$\Delta y = y_+ - y \quad (2.7)$$

5. The next step involves the calculation of an intensity correction factor for the distorted pixels. As a consequence of geometric distortions, intensity distortions also occur. Assuming that the functions in equation (2.1) are invertible, we can substitute the integration variables in equation (2.3) which becomes::

$$C_+(y_+(y)) = \int_0^y I_+(y_+(Y)) \frac{\partial y_+(Y)}{\partial Y} dY$$

$$\text{And } C_-(y_-(y)) = \int_0^y I_-(y_-(Y)) \frac{\partial y_-(Y)}{\partial Y} dY \quad (2.8)$$

Let us not forget that $C_+(y_+(y)) = C_-(y_-(y)) = C(y)$. By taking the derivative, the following equation is obtained:

$$I_+(y_+(y)) \frac{\partial y_+(y)}{\partial y} = I_-(y_-(y)) \frac{\partial y_-(y)}{\partial y} = I(y) \quad (2.9)$$

Defining the two Jacobians

$$\varphi_+(y) = \frac{\partial y_+(Y)}{\partial Y} \text{ and } \varphi_-(y) = \frac{\partial y_-(Y)}{\partial Y} \quad (2.10)$$

Equation (2.9) becomes

$$I_+(y_+(y))\varphi_+(y) = I_-(y_-(y))\varphi_-(y) = I(y) \quad (2.11)$$

And from equation (2.6) we know that

$$y_+(y) = 2y - y_-(y) \quad (2.12)$$

Therefore by taking the derivative with respect to y we obtain

$$\frac{\partial y_+(y)}{\partial y} = 2 - \frac{\partial y_-(y)}{\partial y} \quad (2.13)$$

From (2.10) it follows that

$$\varphi_+(y) = 2 - \varphi_-(y) \quad (2.14)$$

Finally, by inserting the above into equation (2.11) we obtain:

$$\varphi_-(y) = \frac{2I_+}{I_+ + I_-} \text{ and } I(y) = \frac{2I_+ I_-}{I_+ + I_-} \quad (2.15)$$

$I(y)$ is the new value of intensity for the corrected image.

6. With the DM from equation (2.7) and the new intensities for each pixel from equation (2.15) the undistorted image can be calculated.
7. This preliminary corrected image is used to generate a mask to remove regions of low intensity from the DM. Calculation of pixel displacement in these regions is susceptible to errors due to noise.
8. In order to estimate the new displacement values for the regions of low intensity, the masked DM is fitted to a smooth 2D surface. We assume that the magnetic field variations that cause image distortions are smooth across the sample and, therefore, the pixel displacement in regions of low signal intensity should be consistent with their neighboring regions and could be represented by a 2D polynomial surface. The surface is estimated by using a piecewise spline interpolation over several lattices of points. The estimated surface is combined with the masked DM to generate the final DM.
9. Gaussian smoothing is applied to alleviate eventual discontinuities.
10. Finally, using the new DM and the intensity from equation (2.13) the corrected image is generated.
- 5.* In DTI, every slice is acquired a certain number of times. First with no diffusion weighting ($b = 0 \text{ smm}^{-2}$) and then with diffusion weighting (in this case $b = 1000 \text{ smm}^{-2}$) according to the number of gradient directions used (15 directions). Here we assume that the susceptibility distortions are independent of the diffusion gradients. Therefore, the DM is the same for the b_0 image and the diffusion weighted images. For the following explanation, the diffusion weighted image will be noted as \tilde{I} .

For the diffusion weighted images we can write the same equations. From equation (2.11) it follows that

$$\tilde{I}_+ \tilde{\varphi}_+ = \tilde{I}_- \tilde{\varphi}_- = \tilde{I} \quad (2.16)$$

To save time during acquisition, if we acquire the entire DTI dataset for the “+” image (b0 image I_+ and all the diffusion weighted images \tilde{I}_+) and partial DTI dataset for the “-” image (b0 image I_-) we will need to estimate \tilde{I}_- by other means in order to calculate the intensities for the undistorted images. From (2.16) it follows that

$$\tilde{I}_- = \tilde{I}_+ \frac{\tilde{\varphi}_+}{\tilde{\varphi}_-} = \tilde{I}_+ \frac{\varphi_+}{\varphi_-} \quad (2.17)$$

Then, for the diffusion weighted images, equation (2.15) becomes

$$\tilde{I} = \frac{2\tilde{I}_+\tilde{I}_-}{\tilde{I}_+ + \tilde{I}_-} = \frac{2\tilde{I}_+}{\tilde{I}_+/\tilde{I}_- + 1} = \frac{2\tilde{I}_+}{r + 1} \quad (2.18)$$

With

$$r = \frac{\tilde{\varphi}_-}{\tilde{\varphi}_+} = \frac{\varphi_-}{\varphi_+} = \frac{I_+}{I_-} \quad (2.19)$$

A Matlab interface was developed for distortion correction and data analysis (Figure 2.4). Each function module in the interface corresponds to one or several steps of the algorithm described above. Step 1 corresponds to the first function module (“1. Import Data from Archimed” - Archimed is the database used by the laboratory, where the images are stored) where the two images are given as input. Steps 2-10 correspond to the second function module (“2. Reversed Gradient Correction”). Here the user can choose to skip both the sigmoid fit and the surface fit (steps 3, 7-10) by selecting “original method”; or choose to skip only the sigmoid fit (step 3) by selecting “Surface Fit”; skip only the surface fit (steps 7-10) by selecting “Sigmoid Fit” or skip none of the steps described above by choosing “Sigmoid+Surface Fit”. These 4 methods (“Original”, “Sigmoid”, and “Surface”, “Surface + Sigmoid) are then compared in the other panels of the interface. Both visual and statistical comparison is performed (“3. Corrected”, “4.Stats”). A more detailed description of the interface is given in the user manual in Appendix I.

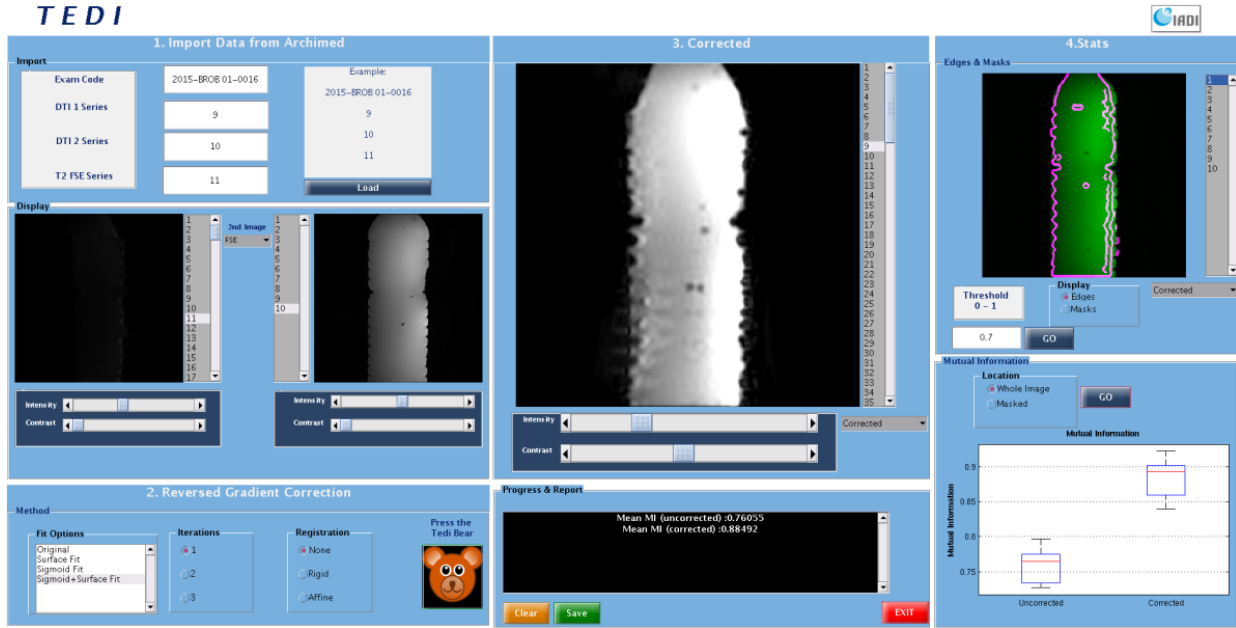


Figure 2.4 – Matlab interface for EPI distortion correction and data analysis. The interface is organized in 4 main panels: “1. Import Data from Archimed”; “2. Reversed Gradient Correction”, “3. Corrected”; “4. Stats”.

2.3.4 Data analysis

Image distortions: Before and after distortion correction, the DTI images were compared to the T2 FRFSE images. First, a visual inspection was performed by superimposing the two images, their respective edges and masks. First, Matlab’s function “edge” was used for edge detection in order to obtain the contours of the images. Then, the contours were superimposed with the T2 FRFSE images Matlab’s function “imfuse”.

For statistical comparison, the mutual information (MI), a measure of similarity between two variables, was computed between the DTI images and the T2 FRFSE images. MI is based on the concept of information theory and expresses the amount of information that one image X contains about a second image Y and it is defined as [52, 53]:

$$MI = H(X) + H(Y) - H(X, Y) \quad (2.20)$$

Where:

$$H(X) = -\sum_x p_X(x) \log p_X(x) \quad ; \quad H(Y) = -\sum_y p_Y(y) \log p_Y(y) \quad (2.21)$$

$$H(X) = -\sum_x p_{XY}(x, y) \log p_{XY}(x, y) \quad (2.22)$$

Here, p_X and p_Y are the probabilities associated with the distributions of pixels in images X and Y respectively and p_{XY} is the joint probability associated with the distribution of pixels of both images simultaneously [52, 53].

The Wilcoxon test was used for a slice-by-slice pairwise comparison of MI. The data was organized as shown in Table 2.3 and the comparison is performed between the columns.

Table 2.3 - Organization of the data for the comparison of mutual information.

<i>Slice</i>	<i>Method of correction</i>			
	Uncorrected	No fit	Sigmoid fit	Sigmoid + Surface fit
<i>1</i>	MI	MI	MI	MI
<i>2</i>	MI	MI	MI	MI
<i>3</i>	MI	MI	MI	MI
<i>:</i>	MI	MI	MI	MI
<i>N</i>	MI	MI	MI	MI

DTI metrics: During the course of the study the phantom was kept in the MRI room to maintain a relatively stable temperature. Regions of interest were placed in the fiber bundles and using the equations from the DTI model, relevant metrics such as ADC and FA computed in Matlab and analysed over a period of four months to test the stability, robustness and reproducibility of the phantom. The Kruskal-Wallis test was used for comparison between five scans.

Finally, fiber tractography was performed using the streamline tracking technique (STT) [56]. This technique assumes that the main eigenvector represents the principal direction of diffusion in each voxel and therefore the direction of the fibers. A starting region of interest (seed ROI) was defined and streamlines were computed between adjacent points until one or both «the stopping criteria were met, either the angle of the fibers exceeded a pre-defined value of 70° or the FA value

was smaller than a threshold of 0.2. A software (DTI search) [54] for Matlab was adapted for this dataset and fiber tractography was computed before and after distortion correction.

2.4 Healthy volunteer studies

The same protocol was applied to human data and images from five healthy volunteers covering the cervical and thoracic spine were obtained but three were discarded due to subject motion. The effectiveness of the correction method was tested with this data.

3 RESULTS

3.1 Coil decoupling

Several coil configurations were tested to determine the optimal coil configuration for imaging different regions of the spine.

Figure 3.1 shows boxplots of the SNR calculated in each channel (only 4 channels are shown) with the first two coil configurations shown in Table 2.1, using groups 1-2 without the chest and face groups, or using groups 1-2 with the chest and face groups.

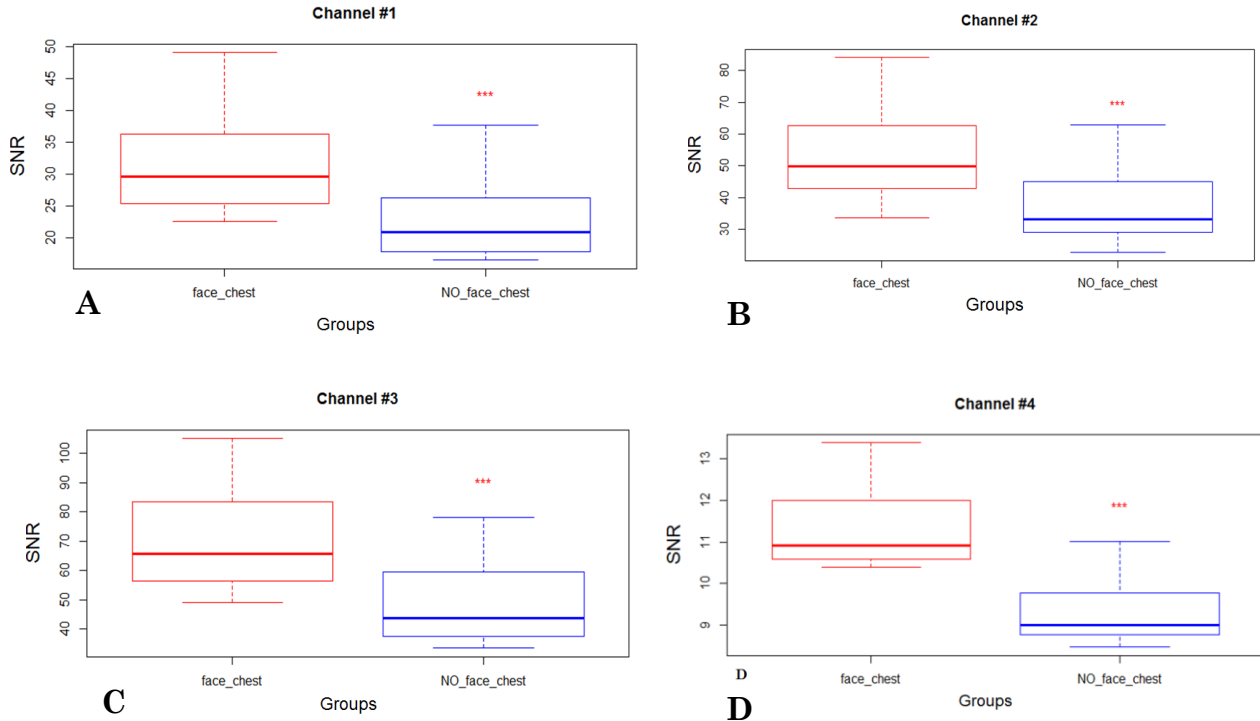


Figure 3.1 - Signal-to-noise ratio in four channels when two coil configurations are used. The red boxplot represents the coil configuration with groups 1-2 and with the chest and face elements. The blue boxplot corresponds to the coil configuration with groups 1-2 and without the face and chest elements. **A:** Channel 1; **B:** Channel 2; **C:** Channel 3; **D:** Channel 4. The boxplots represent values of SNR in 20 slices. The Wilcoxon test was used for a paired comparison between the two coil configurations. The asterisks represent the result of the test, *** ($1.4 \times 10^{-5} \leq \text{p-value} \leq 0.0013$).

The SNR in each channel is significantly higher when the face and chest groups are coupled to groups 1-2. The Wilcoxon test gives p-values smaller than 0.001. Furthermore, channel number 3 shows higher SNR, with a mean of 71 ± 17 with the chest and face elements and 50 ± 14 without the chest and face elements.

Knowing that by having the chest and face elements connected, higher SNR could be achieved, the following step was to keep the face and chest groups and study the SNR while progressively adding other groups (1-2-3-4-5-6). Figure 3.2 shows boxplots of SNR in 7 channels. Only 7 channels are shown because when only segments 1-2 are connected, 7 channels are acquiring signal. When segments 1-2-3 are connected, 9 channels are acquiring signal and when segments 1-2-3-4 are connected 11 channels are acquiring signal. Therefore, in order to compare the SNR for different coil configurations, only the channels (1 through 7) that are always acquiring signal can be considered. For clarification purposes, it is also worth noting that the segment number does not necessarily correspond to the channel number.

Here the Wilcoxon test was performed two-by-two between the three coil configurations shown in Figure 3.2. It is evident that there is a significant decrease of SNR in the channels when the number of segments that are acquiring signal increases. For all the channels there is a significant decrease of SNR from configuration 1-2 to configuration 1-2-3 with p-values between 2.9×10^{-6} and 0.0019. The same happens when we compare configuration 1-2 with configuration 1-2-3-4 with p-values between 2.2×10^{-5} and 0.001.

Comparing configuration 1-2-3 with configuration 1-2-3-4 there is also a significant decrease of SNR in channels number 2, 3, 6 and 7 when increasing the number of elements.

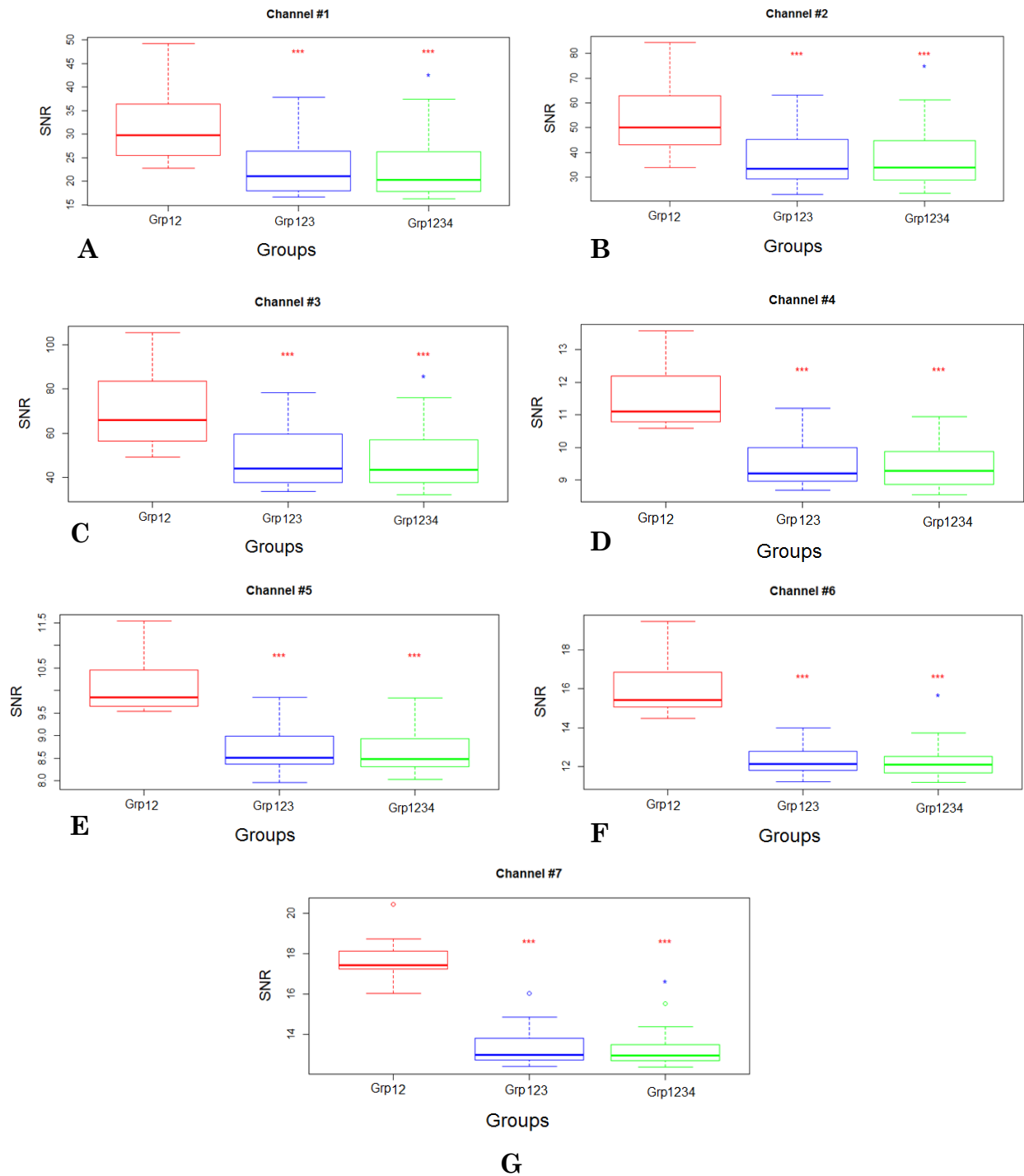


Figure 3.2 - Signal-to-noise ratio in seven channels for different coil configurations when the chest and face elements are connected. The red boxplot corresponds to groups 1-2, the blue corresponds to 1-2-3 and the green corresponds to 1-2-3-4. The boxplots represent values of SNR in 20 slices. The asterisks mark the result of the Wilcoxon test performed pairwise between the three boxes. Red asterisk over the blue plot is the result between the blue and red boxes; Red asterisk over the green box is the result between the green and the red boxes; Blue asterisk over the green box is the result between the green and blue boxes; * (p-value < 0.05); *** (p-value < 0.001); When no asterisks are present it means that there is no significant difference.

3.2 Distortion correction

An important issue to take in account with DTI images is the intensity and geometric distortions caused by field inhomogeneities. In the correction method described in section 2.4.3, the calculation to the displacement map is divided in several steps.

One of the most important steps (steps 2 - 3) is the calculation of the CDF and respective fitting to a sigmoid function. Figure 3.3 A and B shows examples of the result of the CDF of the I+ image before and after sigmoid fit, respectively. The curves are smoother after the fit. Figure 3.3 C and D shows the comparison of the CDF from one line (128) in the I+ and the I- image. The two curves present similar shapes but in some regions there are slight differences. In this correction method it is assumed that the CDFs of the two images have the same shape, with the only difference being the displacement of these curves relative to a central point.

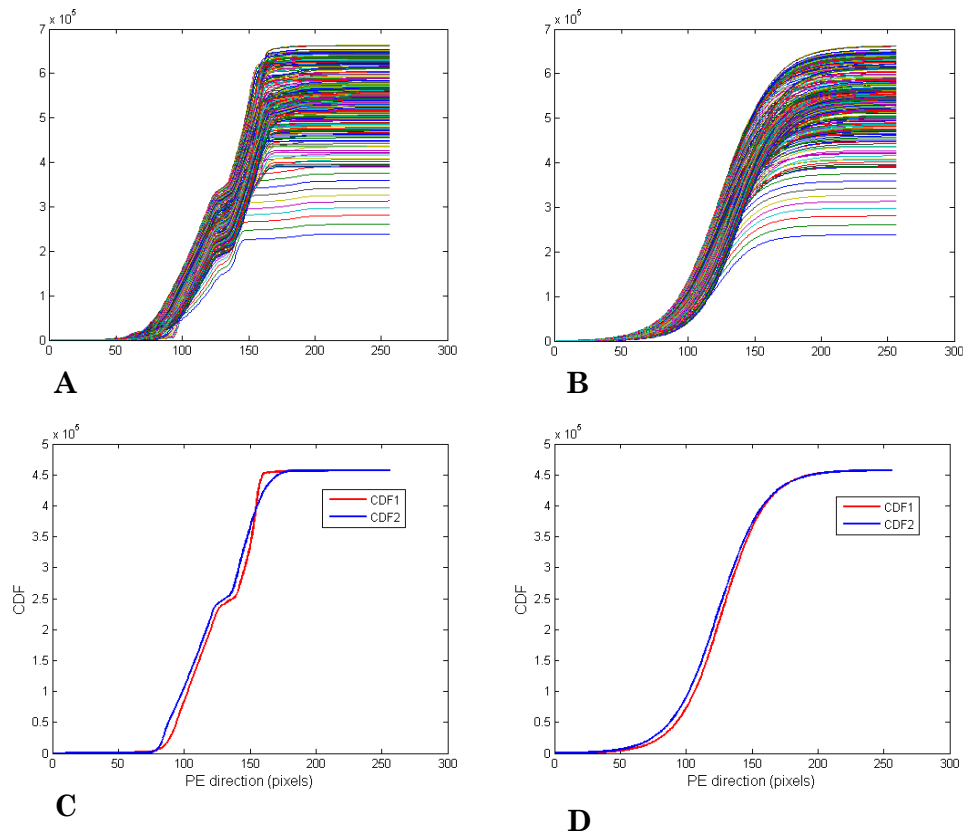


Figure 3.3 - Cumulative distribution function. **A, B:** CDFs of one slice in the I + image before and after sigmoid fit, respectively. Each curve is represents the CDF from one line of the image. Note the smoothness of the curves after the fitting. **C:** CDF of one line (128) in the I+ image (in red) and in the I- image (in blue) before the sigmoid fit; **D:** CDF of the same line after sigmoid fit.

The root mean square error (RMSE) was calculated between the CDF+ and CDF- before and after sigmoid fit and the result is shown in Figure 3.4:

$$RMSE = \frac{\text{mean}(\sqrt{(cdf^+ - cdf^-)^2})}{\text{mean of all the obs}} \quad (3.1)$$

Here cdf^+ and cdf^- are the two CDF curves being compared.

The results show that the RMSE between the two curves decreases after the sigmoid fit (p-value of Wilcoxon test, <0.001), indicating that the discrepancies between the curves are minimized.

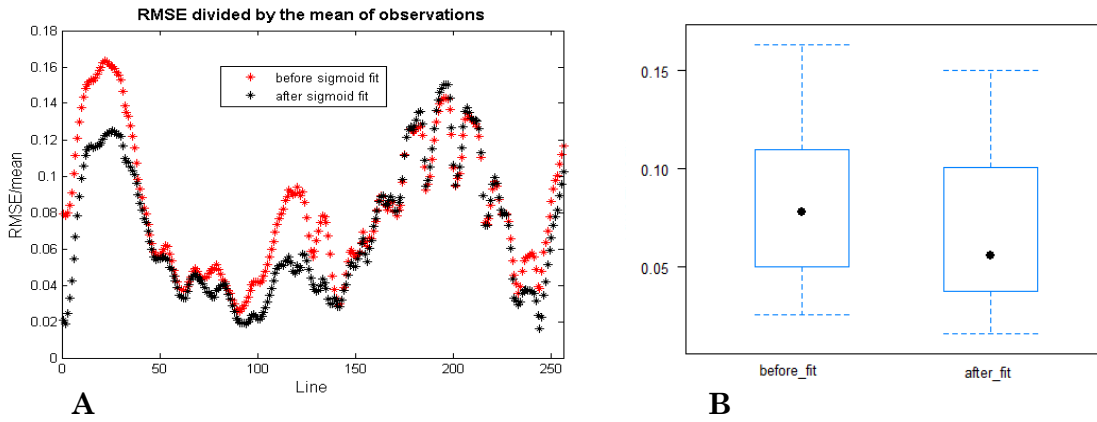
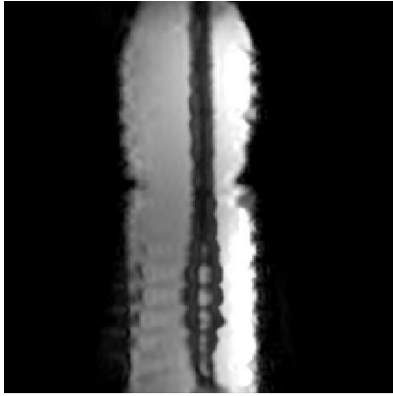


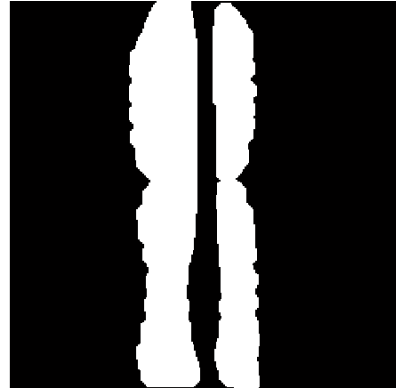
Figure 3.4 - RMSE between the CDF+ and CDF- before and after sigmoid fit. **A:** Each point is the RMSE between one CDF+ line and its corresponding CDF- line shown in Figure 3.3. Note that one slice has 256 lines, therefore 256 values of RMSE are calculated. **B:** Boxplot representation of the values shown in A.

The next step (steps 4-10) was the calculation of the DM and respective fitting of a polynomial surface. In this step, DM regions of the image with low signal intensity where calculation errors may occur are removed from the map and their values are estimated from the polynomial surface. The final DM is the combination of the original map (regions of high signal) with the surface (regions of low signal). To remove the regions of low signal, a preliminary image was calculated and a mask was computed from it (Figure 3.5 A and B). This preliminary corrected image is still not the desired result since some regions are inaccurately represented.

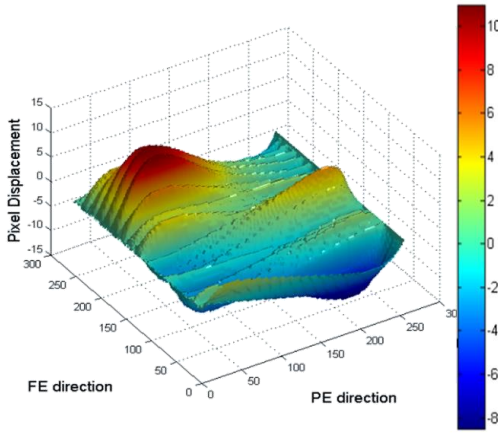
After surface fit, the result is a displacement map with smooth variations between nearest-neighbor regions (Figure 3.5 F).



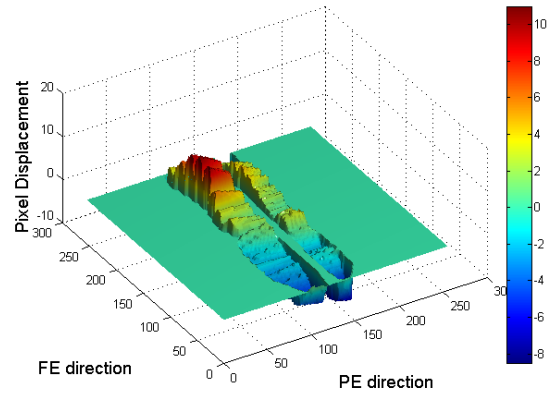
A



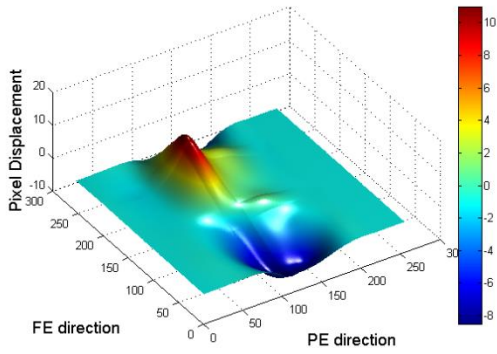
B



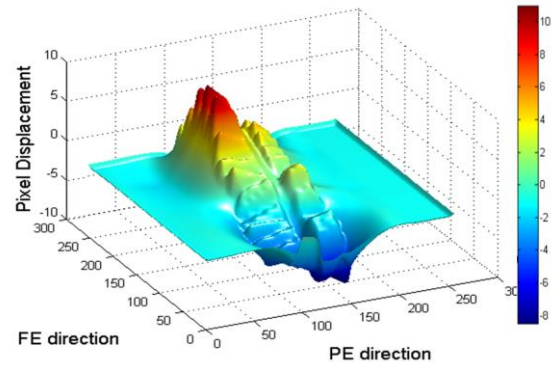
C



D



E



F

Figure 3.5 - A - Preliminary corrected image used to generate a mask; B - Mask; C - Original displacement map calculated from the CDF; D - DM with regions of low signal intensity removed; E - DM fitted to a polynomial surface; F - Final displacement map.

Figure 3.6 shows the images before distortions correction (step 1). The two DTI-EPI images (only the b0 acquisition is shown) with opposite phase encoding directions have distortions in opposite directions in the PE axis. The third image is a distortion free T2 FRFSE, which is a more reliable representation of the phantom.

When the contour of the images is superimposed with the T2 FRFSE image, it is evident that the distortions are more severe in the edges of the bottle. The fine details in the edges are distorted and not accurately represented. Some regions of the fiber bundles, especially the top and bottom, are also affected, showing curvatures that do not exist in the physical phantom.

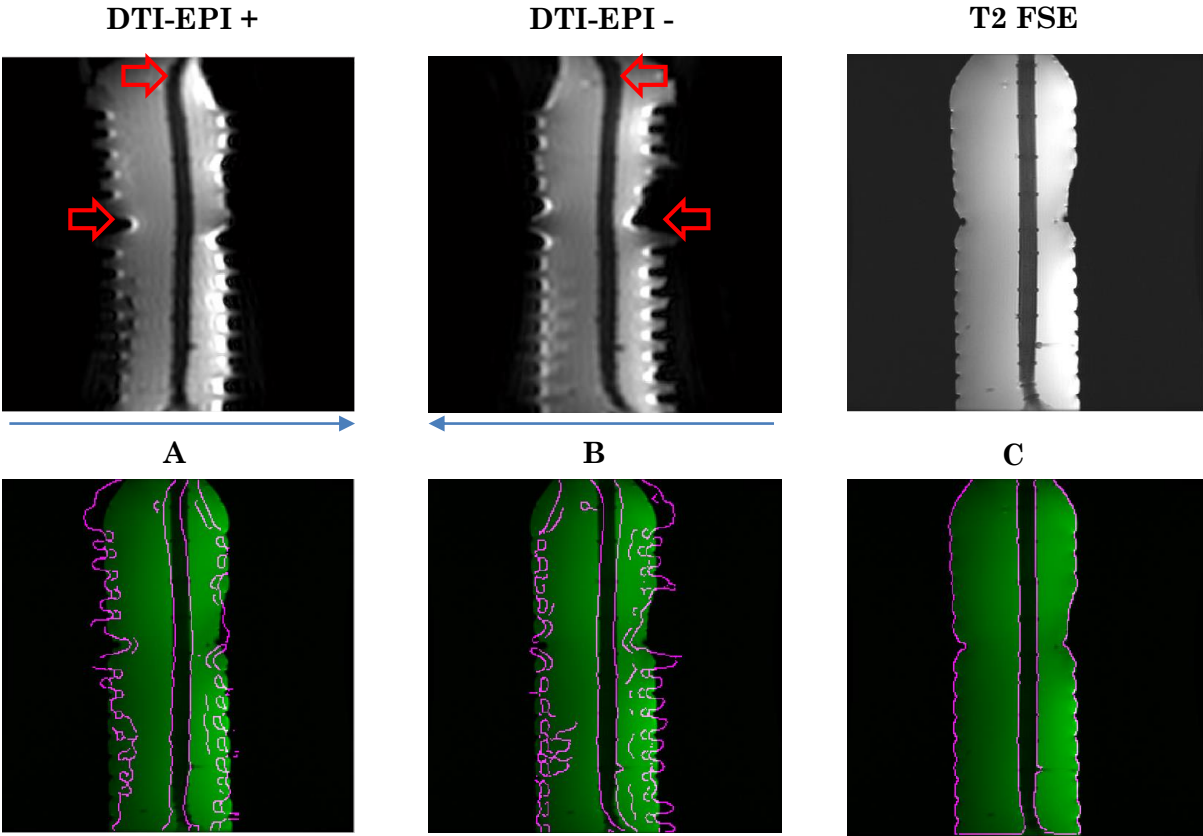


Figure 3.6 - Top: A: DTI-EPI dataset with anterior-posterior phase encoding direction (blue arrow); **B:** DTI-EPI dataset with posterior-anterior phase encoding direction (blue arrow), the + and - symbolically indicate the PE direction; **C:** Distortion-free T2 FRFSE image. **Bottom: A:** Contour (in magenta) of the DTI-EPI+ image superimposed to the T2 FRFSE; **B:** Contour of the DTI-EPI- image superimposed to the T2 FRFSE; **C:** Contour of the T2 FRFSE superimposed to the respective image. Red arrows indicate regions presenting higher distortions.

Figure 3.7 shows the result after distortion correction. When no fitting is applied (by skipping steps 3, 5-9), the correction method is able to minimize the distortions in the edges of the bottle. However, the method fails in regions of low SNR such as the fiber bundles. The same problem still occurs when the CDF are fitted to a sigmoid function before the estimation of the displacement maps, but the surface fit is skipped (steps 5-9 are skipped). When these low SNR regions are removed from the DM and fitted to polynomial surface (none of the steps are skipped), the final result is a more accurate representation of the phantom. The distortions in the edges of the bottle are minimized, as well as in the regions of the fiber bundle that present a straighter shape. Visual inspection of the contours of the corrected images superimposed to the T2 FRFSE confirms the results mentioned above

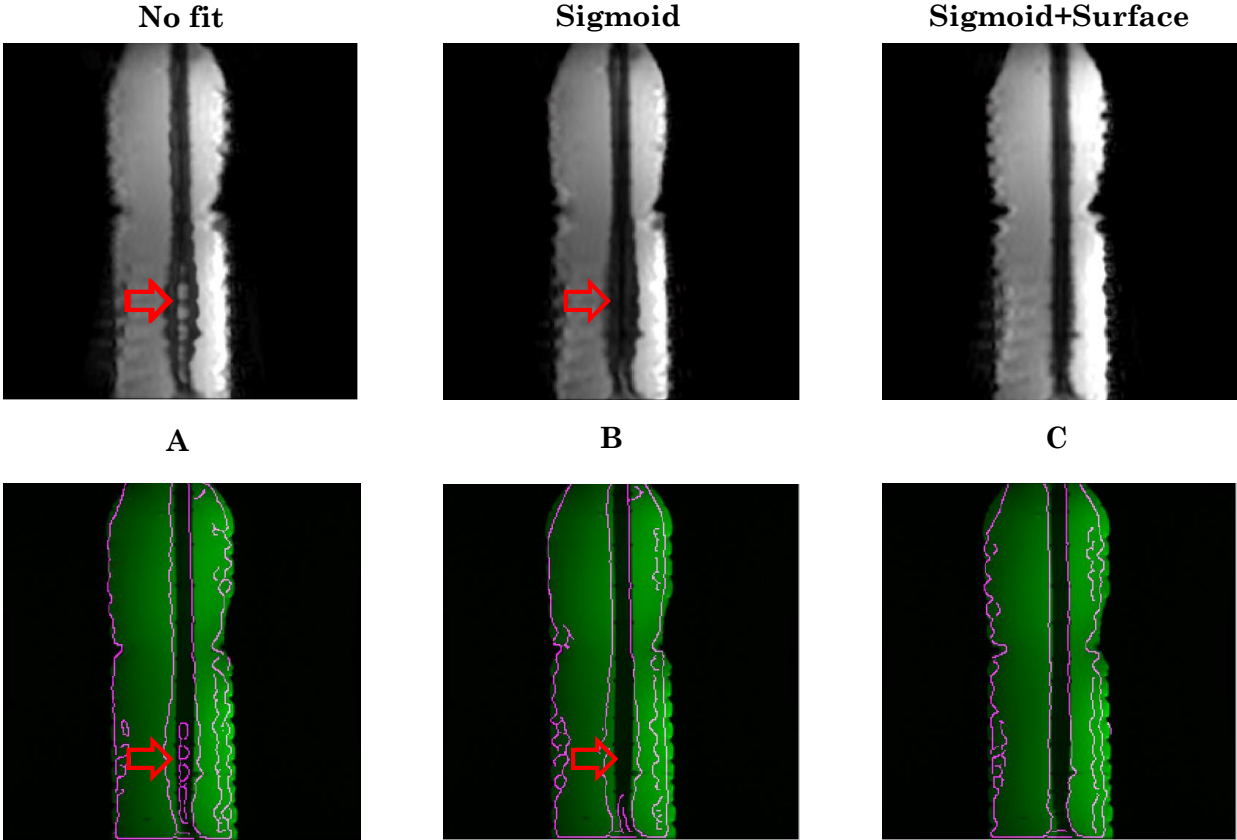


Figure 3.7 - Top: A: DTI-EPI after distortion correction using the original method with no fitting; **B:** Result after distortion correction using only the sigmoid fit; **C:** Result when using both the sigmoid and surface fit in the correction method. **Bottom:** Contour of the images on the top superimposed to the distortion free T2 FRFSE images. Red arrows indicate regions of low SNR where the correction fails.

The MI, a measure of similarity between two images, was calculated between the DTI-EPI image and the distortion free T2. The boxplots represent the MI calculated in all slices.

Figure 3.8 shows that there is a lower similarity between the DTI-EPI and the T2 FRFSE images when no correction method is used. After distortion correction there is an increase of similarity, independently of the method used. However, there is a high variability (size of the boxplots) between the slices when different correction methods are used. The Wilcoxon test shows a significant difference in MI when no correction method is used, i.e. the comparison of the red boxplot with all the others result in p-values between 0.015 and 0.022. No significant differences in MI were found between the correction methods.

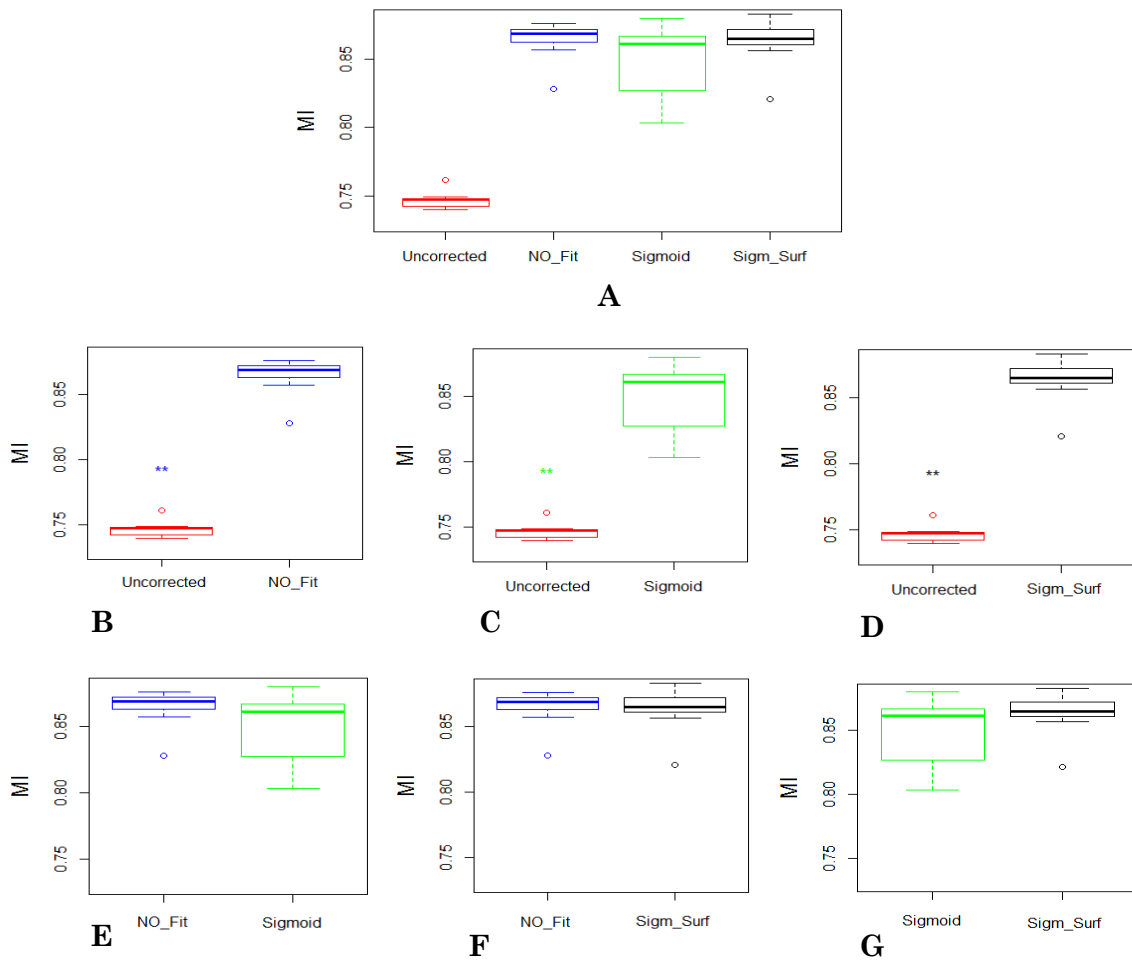


Figure 3.8 - Mutual information between the DTI-EPI and T2 FRFSE images. **A**: Boxplot representation of the MI before and after distortion correction with different methods. **B-G**: Pairwise comparison between the boxplots; The Wilcoxon test was used; the asterisk represent the result of the test, ** ($0.015 \leq p\text{-value} \leq 0.022$). No asterisks are shown when the p-value > 0.05 .

Figure 3.9 to 3.12 show the fiber tracts computed using the STT technique before and after distortion correction, respectively. Before distortion correction (Figure 3.9), a curvature is present in the fiber tracts and in some regions the fibers are misrepresented. If no fitting is used in the correction method (Figure 3.9, the STT fails to extract the fibers correctly, since these low SNR regions are corrupted after correction. The same problem still persists when only the sigmoid fit is used in the correction method (Figure 3.11). When both the sigmoid and surface fits are used (Figure 3.912), the curvature is minimized and the tracts display a straighter shape, a more reliable representation of the physical phantom.

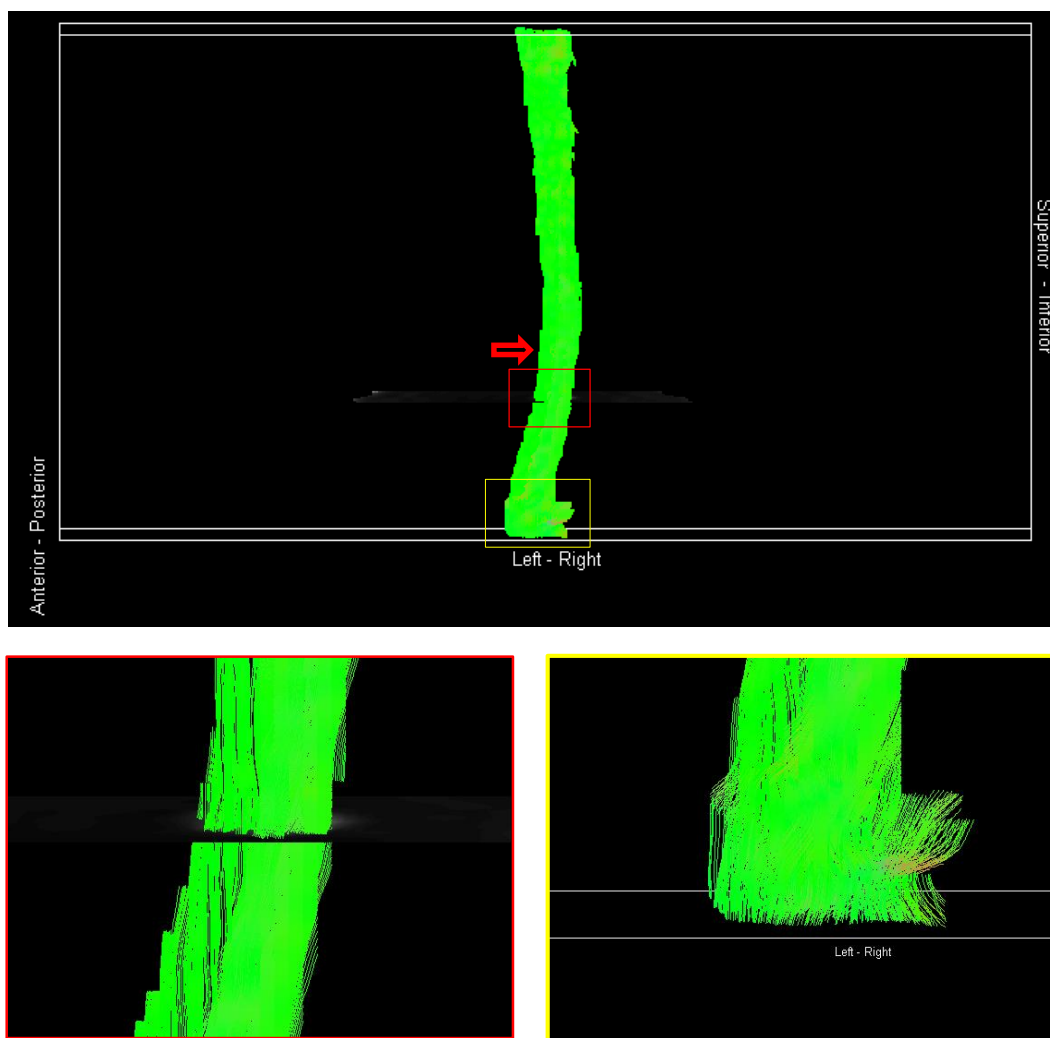


Figure 3.9 - Fiber tracts computed with the STT technique before distortion correction. Red arrow indicates a curvature in the fiber tracts due to distortion. Red and yellow boxes indicate the regions that were amplified and shown in the bottom images. The left image shows the seed ROI where the fiber tracking begins. The right image shows a region where errors in fiber tracking occur.

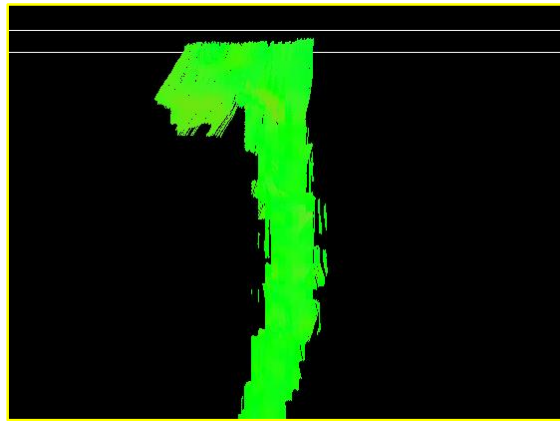
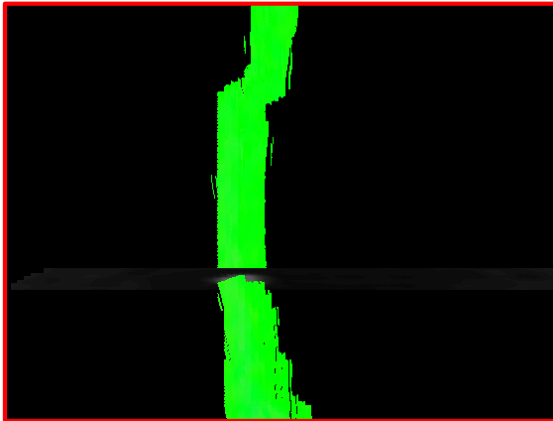
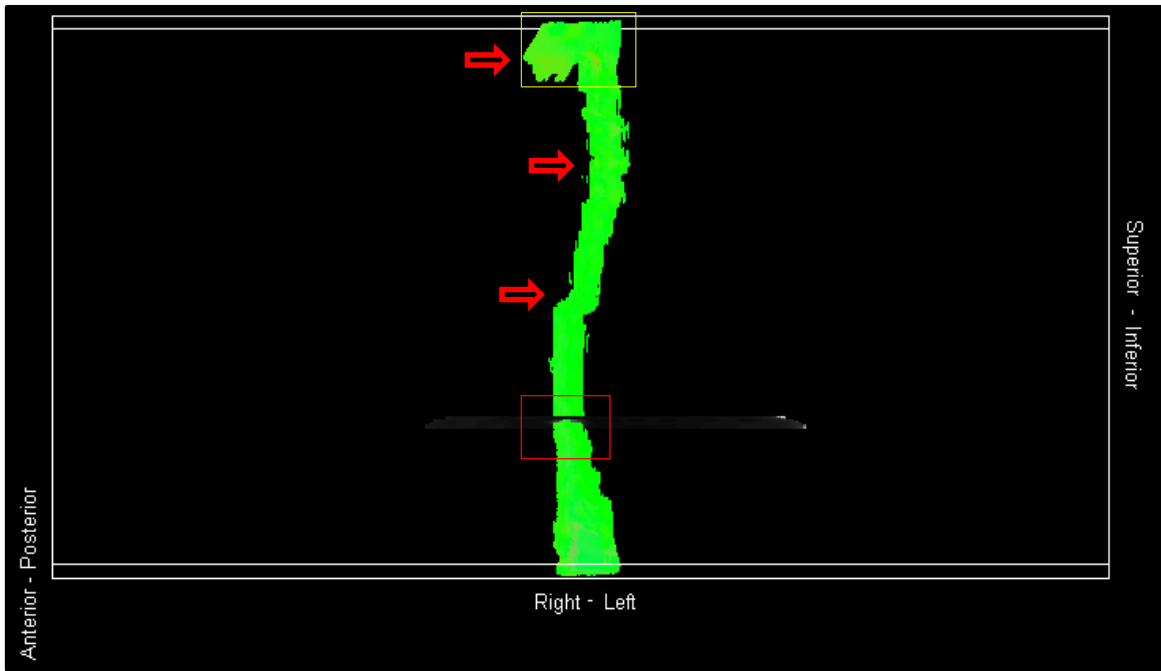


Figure 3.10 - Fiber tracts computed with the STT technique after the correction with the original method (without sigmoid or surface fit). Red arrow indicates a curvature in the fiber tracts due to distortion. Red and yellow boxes indicate the regions that were amplified and shown in the bottom images. The left image shows the seed ROI where the fiber tracking begins. The right image shows a region where errors in fiber tracking occurs.

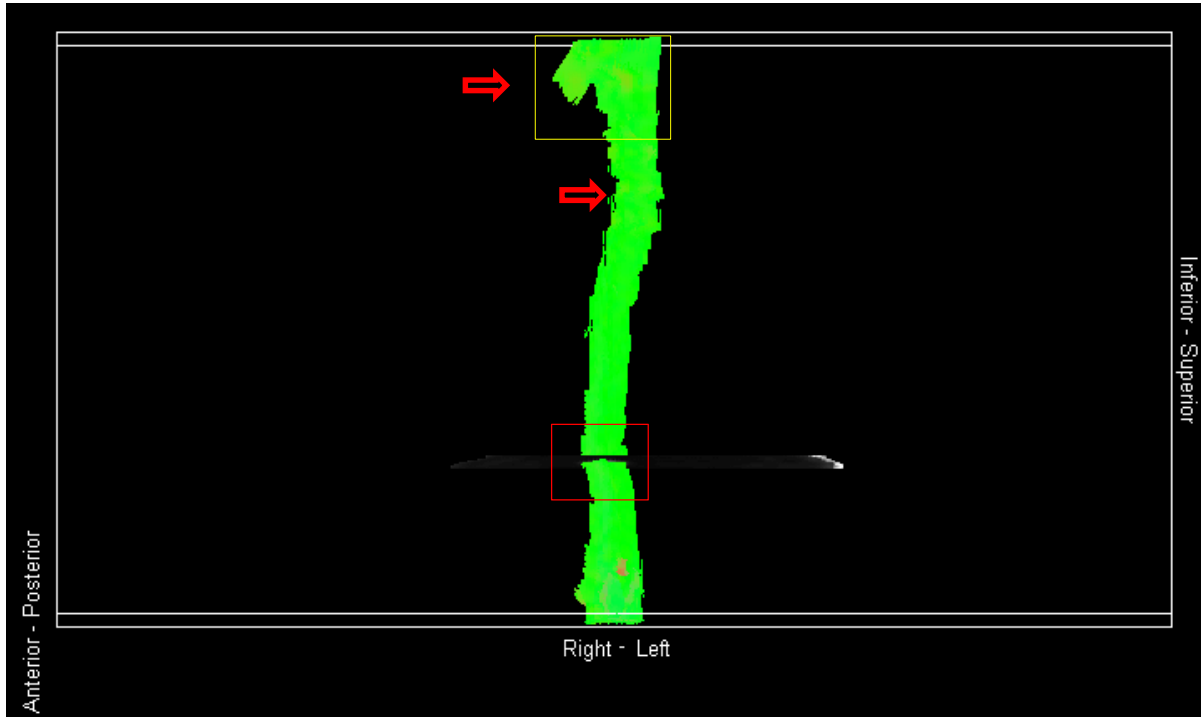


Figure 3.11 - Fiber tracts computed with the STT technique after distortion correction using only the sigmoid fit. The curvature present in the figures is minimized. Red and yellow boxes indicate the regions that were amplified and shown in the bottom images. The left image shows the seed ROI where the fiber tracking begins. The right image shows a region where errors in fiber tracking occurred in the previous case.

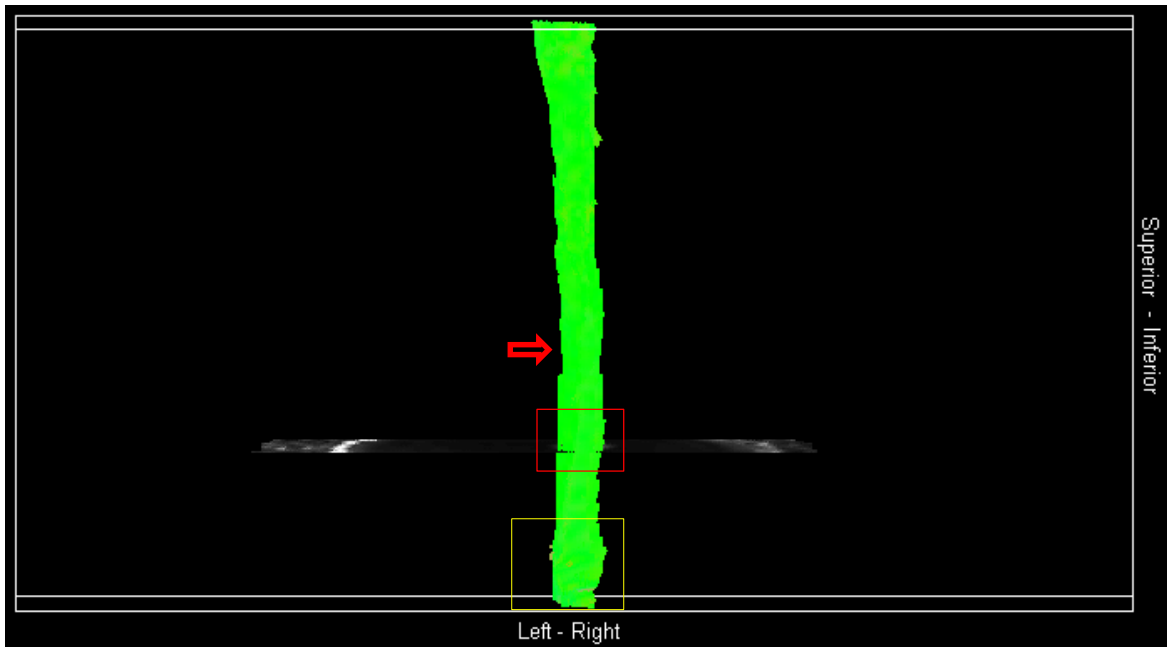


Figure 3.12 - Fiber tracts computed with the STT technique after correction using both the sigmoid and surface fits. The curvature present in the figures is minimized. Red and yellow boxes indicate the regions that were amplified and shown in the bottom images. The left image shows the seed ROI where the fiber tracking begins. The right image shows a region where errors in fiber tracking occurred in the previous case.

3.3 DTI metrics

DTI maps were computed from the diffusion weighted images. Figure 3.13 show the FA map in ten slices. It is clear that anisotropy was achieved inside the bundle of fibers, with FA being higher in this region. Here diffusion is predominant in the direction parallel to the fibers orientation as show by Figure 3.13 B. This color-coded map represents the direction of the main

eigenvector weighted by the value of FA. The fiber bundle has a red color, indicating that water molecules are moving preferentially in the up-down direction.

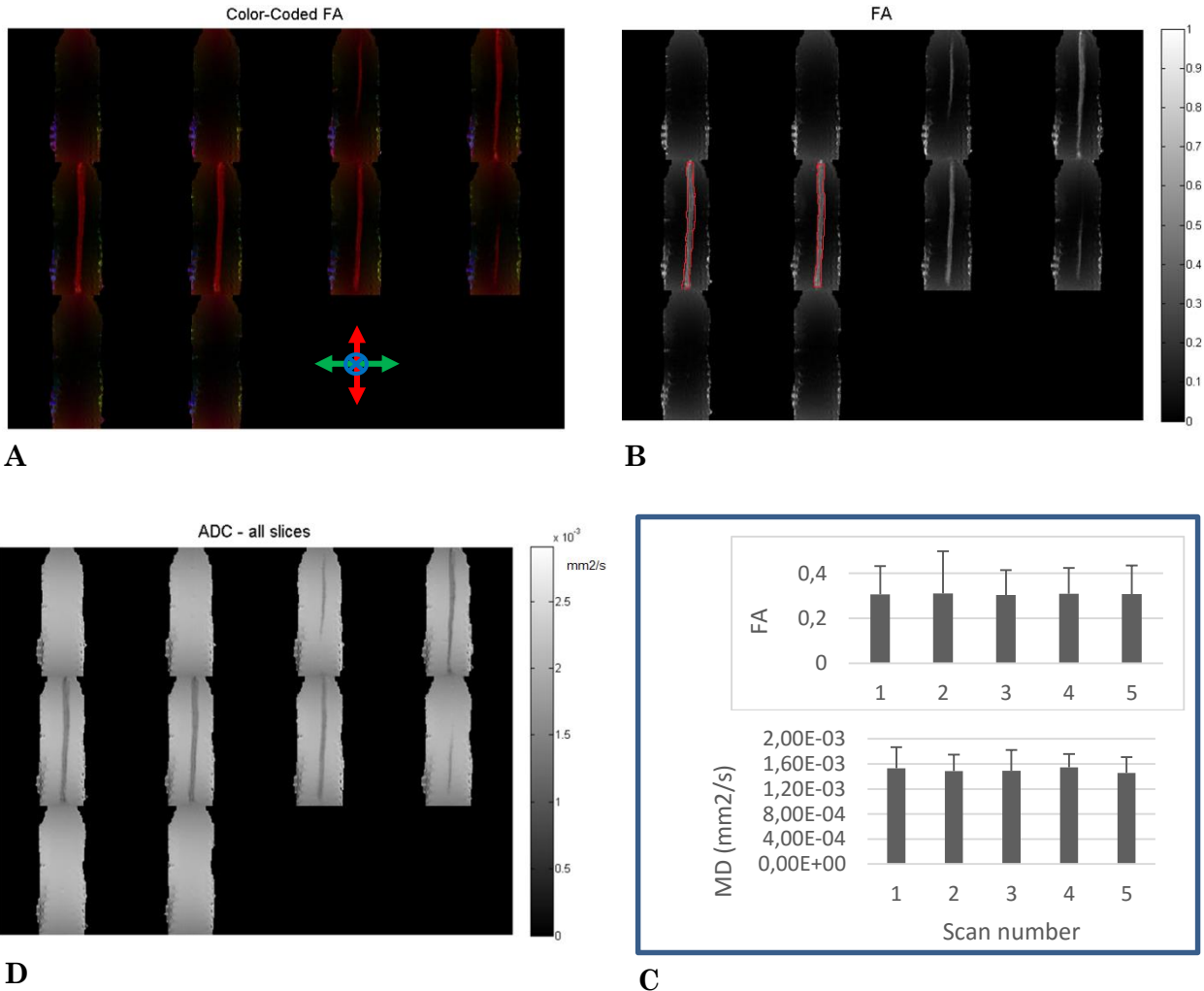


Figure 3.13 - A: Color coded FA map. The colors are defined by the direction of the main eigenvector and the amplitude is weighted by FA. Note the color code given by the arrow system. Diffusion in the up-down direction is represented in red; Left-right is represented in green, and finally inwards-outwards of the plane is represented by blue. **B:** FA maps of ten slices. The fiber bundle show higher values. Note the ROI placement (in red) for the measurement of FA and ADC. **C:** ADC maps. Regions containing free water have higher values. **D:** FA and ADC values in the fiber bundle over a period of 4 months. The Mann-Wallis test shows no significant difference over time; p-value > 0.6.

Figure 3.13 C represents ADC maps. As expected, ADC is higher in the water surrounding the fiber bundle. Nevertheless, in this region, ADC has the same order of magnitude.

In order to verify the stability and reproducibility of the phantom, ADC and FA were measured several times over a period of 4 months and the result is shown in Figure 3.13 D.

Regions of interest were placed in the fiber bundles and FA and MD values were calculated. A mean FA of 0.38 ± 0.20 and a mean MD of $(1.50 \pm 0.04) \times 10^{-3} \text{ mm}^2/\text{s}$ were obtained. The Kruskal-Wallis test shows no significant difference in these metrics over time ($p\text{-value} > 0.6$).

3.4 Healthy volunteer studies

Figure 3.14 shows images from healthy volunteers before distortion correction. The two EPI images present distortions in opposite directions along the PE axis. These distortions are reflected as sheering and compression of the structures, small undulations along the spine as well as accentuated curvatures that are better displayed when the contour of the EPI images are superimposed to the T2 FRFSE image. Apart from distortion there is also the presence of ghost artifacts.

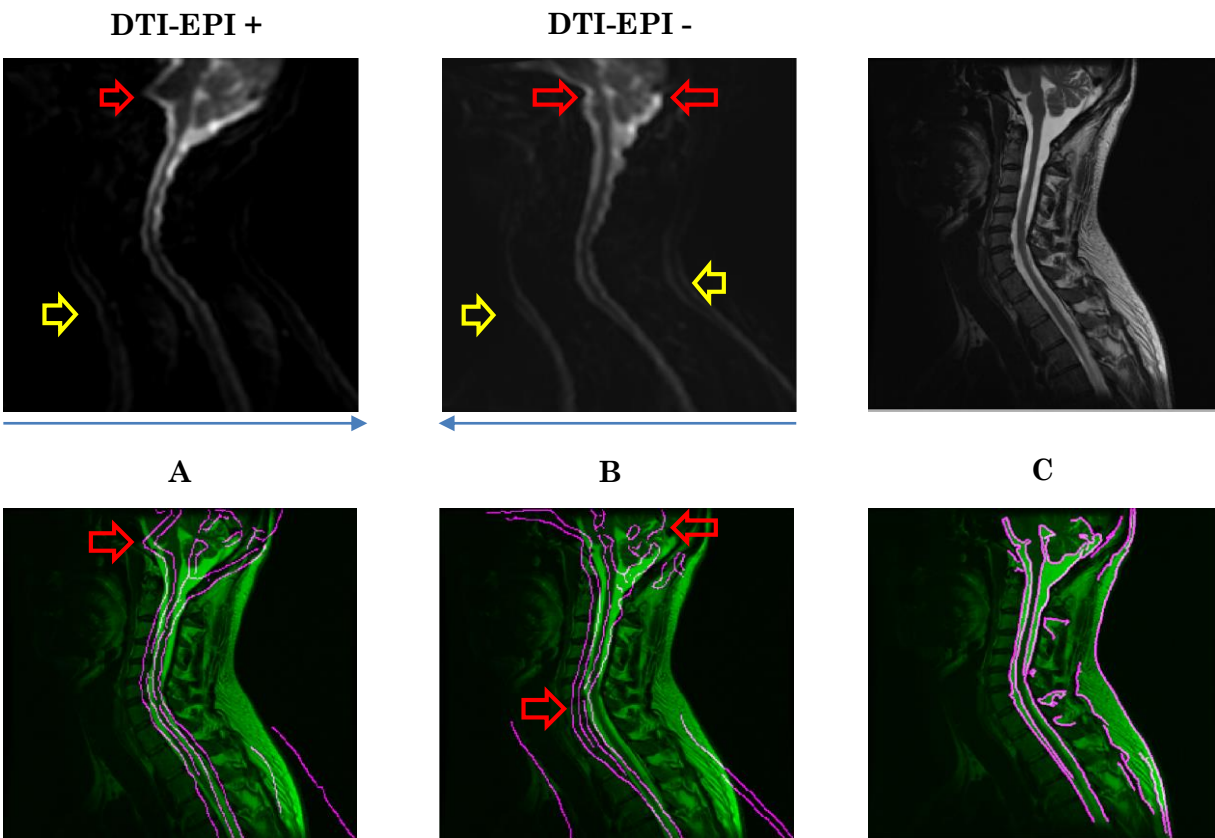


Figure 3.14 - Images from healthy volunteers before correction. **Top: A:** Dataset with left-right phase encoding direction (blue arrow); **B:** Dataset with right-left phase encoding direction (blue arrow), the + and - symbolically indicate the PE direction; **C:** Distortion-free T2 FRFSE image. **Bottom: A:** Contour (in magenta) of the DTI-EPI + image superimposed to the T2 FRFSE; **B:** Contour of the DTI-EPI- image superimposed to the T2 FRFSE; **C:** Contour of the T2 FRFSE superimposed to the respective image. Red arrows indicate distortions. Yellow arrows indicate ghost artifact.

Figure 3.15 shows the same images after correction. None of the methods is able to completely correct the distortions. The three methods are able to correct the distortions in the upper region of the image where ghost artifacts are minimal. However, in the lower regions where ghosting is more severe, the correction is not efficient.

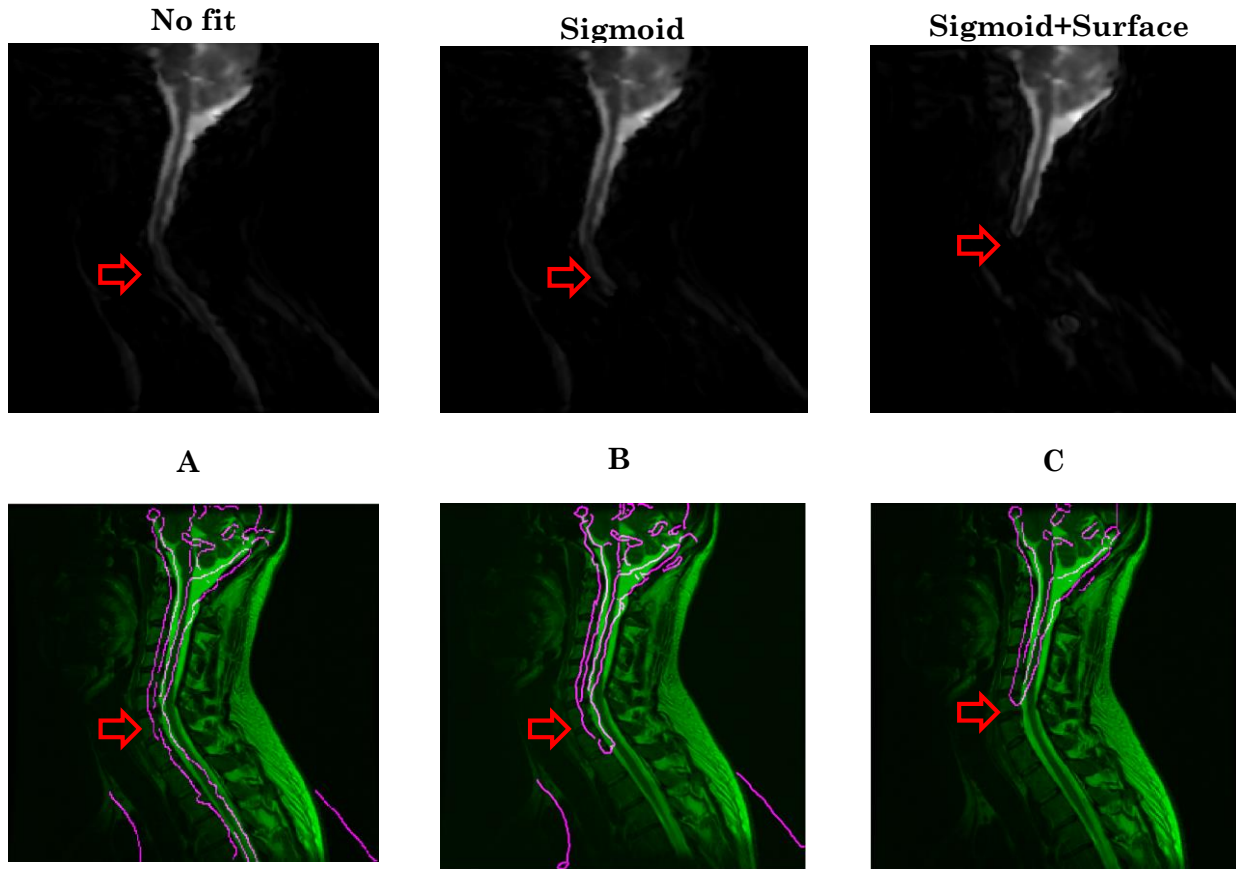


Figure 3.15 - Images from healthy volunteers after correction. **Top A:** Post correction using the original method with no fitting; **B:** Result after distortion correction using only the sigmoid fit; **C:** Result after using both the sigmoid and surface fit in the correction method. **Bottom:** Contour of the images on the top superimposed to the distortion free T2 FRFSE images. Red arrows indicate regions where the correction fails.

4 DISCUSSION

In this work, the first step was to determine the optimal coil configurations for the HNS coil for imaging a structure such as the spinal cord, and also explore the possibilities of using parallel imaging. This was performed with a coil decoupling experiment.

Previous studies [55] show that in a multi-channel or multi-element coil array there can be noise induction or interference of one channel over the other. This can affect the information gathered by each channel. This is relevant when we are interested in applying parallel imaging. With this technique, the information collected by each channel is treated as independent of one another and then combined to produce a final image. The influence of one channel over the other can also be verified by studying the noise correlation matrix between the channels.

This is also relevant in order to determine which coil configuration should be used to image different regions of the spinal cord with this HNS coil. The coil has a total of 29 elements connected to 16 channels and organized in 8 segments (the chest, face, and other 6 segments in the posterior part).

In the upper section of the coil there is the possibility to use the face and chest part in addition to segments 1-2, in order to have a greater coverage of the object of interest. Indeed it was possible to verify that in the channels that were acquiring signal, higher SNR is achieved when using the face and chest parts with groups 1-2 in contrast with the case where they are not used. In order to successfully use parallel imaging, it would be ideal to have coil elements symmetrically distributed over the imaged object. In spinal cord imaging, it is most common to use the anterior-posterior direction as the PE direction since no aliasing of the shoulders and other structures would occur over the spine. With this coil, the distribution of elements in the PE direction is relatively symmetrical in the upper region where there are elements in the anterior and the posterior part of the spine. This means that parallel imaging is possible in the upper section of the spine covered by groups 1-2-3, the face and chest parts. Therefore it is advantageous to use the chest and face parts, not only because of the increase of SNR but also due to the fact that it allows parallel imaging for acceleration in the PE direction. In the lower regions, covered only by 4-5-6, parallel imaging would only be possible if the PE direction was cranial-caudal. However, this is difficult to accomplish because the phase FOV cannot cover the entire extent of the spinal cord which means that the regions outside of the FOV would suffer aliasing.

Knowing that the SNR is higher when using the face and chest parts, the next step was to keep these parts connected and add other elements in the posterior section (groups 3-4). As additional elements are used, the SNR in the channels decreases. This may happen because the decoupling circuit between the elements of the coil is not perfect, hence the channels are not totally independent. For example, channels 1 to 7 are only acquiring signal from elements grouped in groups 1-2, chest and face. The signals from elements grouped in groups 3-4-5-6 are acquired by other channels. However, when these elements are connected, their noise also contributes to the decrease in SNR in channels 1 to 7 that do not correspond to them. Thus when imaging specific sections of the spinal cord, for instance the cervical spine, it is preferable to use the minimal number of coil elements. In this case, one should only use groups 1-2, face and chest. The same principle applies to the other sections of the spine. If bigger FOVs are intended when imaging larger portions of the spine, this can be achieved by using more elements at the same time, with a cost in SNR.

The next step in this work was the improvement of distortions in DTI images caused by static field inhomogeneities. The algorithm used is based on a method that estimates the pixel displacement map from two DTI-EPI images with opposite PE directions. The correct estimation of the DM depends on several factors, including the SNR, the presence of other artifacts apart from distortion (e.g. ghost, motion). One of the assumptions is that the two images, if not affected by other artifacts, differ only in terms of distortions that will have opposite directions. Therefore, their respective CDFs should have similar curves. This is ensured by fitting both CDFs to a sigmoid function before calculating the DM. Moreover, the influence of SNR is minimized by removing regions of low SNR from the DM. The new values of displacement in these regions are obtained from a fitted polynomial surface. Indeed if no surface fit is used, the correction fails in regions of low signal intensity (fiber bundle) due to erroneous estimation of pixel displacement.

In general, the distortions are more severe in the edges of the bottle. The small undulations of the bottle are distorted and unrecognizable from the physical phantom. In fact, in these regions the correction results are slightly better when no fitting is used. This occurs because there is always a loss of information when the original CDF curves and DM are fitted to the sigmoid function and polynomial surface, respectively. Visually, the uncorrected image presents low resemblance with the T2 FRFSE image and this is confirmed by the MI. Statistical analysis shows an increase of MI between the distortion free T2 FRFSE and DTI-EPI images when the correction is applied. However, no significant difference was found between the methods (the original reversed gradient

method with no fitting, with the sigmoid fit and with the surface fit). This is due to the fact that the calculation of MI is based on the entire image. Therefore, the regions where the correction methods differ (low SNR regions) are too small to make a significant difference on the value of MI. Nevertheless, by visual inspection it is clear that using the sigmoid and the surface fit is advantageous for the improvement of the image quality (Figure 3.7). This is emphasized after the estimation of the fiber tracts (Figures 3.9 - 3.12). The fiber bundle is not accurately represented in the uncorrected image or when no fitting is used in the correction method. When only the sigmoid fit is used, the estimation of the fiber tracts is also corrupted because the fiber bundles have low SNR in the DTI images. As mentioned before, the sigmoid fit alone is not sufficient for a correct estimation of the DM in low SNR regions. Only when both the sigmoid and surface fits are used, do the fiber tracts have a more reliable shape and resemblance with the physical fiber bundle.

In order to study the reproducibility and stability of the phantom, FA and ADC maps were calculated over time and their values were measured in ROIs placed in the fiber bundle. The results show that an anisotropic diffusion was achieved inside the fiber bundles, with water diffusing predominantly in the direction parallel to the fibers as expected. The ADC value is within the expected range and the FA value was slightly lower than observed in white matter of the spinal cord (FA between 0.4 and 0.75) [31, 32, 34]. This may be explained by the fact that the phantom is only a simplification of reality. Here, the anisotropic diffusion is only created by the molecules between the fibers (extracellular space). Moreover, diffusion is also dependent on the composition of the fluid and its temperature, which are not the same as in the spinal cord. Nonetheless, the phantom was stable over time and FA and ADC did not display significant variations.

Lastly, the distortion correction method was applied to human data. Images from the brainstem and the cervical spinal cord were obtained. When compared to the T2 FRFSE, the DTI images present distortions mainly along the phase encoding direction. Here, the curvature of the spine is misrepresented. Furthermore, there are ghost artifacts that influence the correction. The method works in regions where ghost artifacts are minimal, but fails in regions where they are more severe. This happens because these artifacts are not the same for the two EPI images. There is no linearity for the ghost artifacts between the two images. For example, in an inverse line of thought, with the DM and the EPI+ image, one can estimate the EPI- image. However, if the EPI+ image has ghosts, it is not possible to correctly estimate the second image. Therefore, when the DM map is estimated from the two EPI images, the pixel displacement values obtained are corrupted because errors occur during the estimation of the CFD.

5 CONCLUSION AND PERSPECTIVES

DTI is gaining relevance in clinical studies including the spinal cord. However, imaging this organ is not straight-forward and many challenges may arise. In longitudinal MR studies with the spinal cord, test-objects are always relevant for the optimization of protocols and methods for the improvement of image quality.

The phantom presented in this work is a simplification of the complex structure of the spinal cord but it was easily constructed with cheap materials and during the course of the study it was a reliable and reproducible object that allowed a continuous optimization of the DTI protocol, coil configurations and improvement of distortion correction method. Moreover, the novelties proposed for the correction method, namely the sigmoid and surface fit, proved to be robust improvement of distortions both in regions of low SNR and regions of higher SNR.

Future work will reside on the improvement of the phantom, with more complex structures (curved shapes and crossing fibers,) that are more accurate representations of the spinal cord. Different fiber dimension and materials can also be explored. As for the correction method, when transposed to human data, other challenges apart from susceptibility distortions, such as ghost artifacts, must also be taken in account in order to improve the robustness of the correction method.

REFERENCES

- [1] J. E. T. E. O. Stejskal, "Spin Diffusion Measurements: Spin Echos in the Presence of a Time Dependent Field Gradient," *JCP*, vol. 42, no. 1, pp. 288-292, 1965.
- [2] "MRI online course (Magnetic Resonance Imaging)," *IMAIOS*. [Online]. Available: <https://www.imaios.com/en/e-Courses/e-MRI>. [Accessed: 07-Dec-2015].
- [3] E. M. Haacke, R. W. Brown, M. R. Thompson, and R. Venkatesan, *Magnetic Resonance Imaging: Physical Principles and Sequence Design*. Wiley, 1999.
- [4] H. Y. Carr and E. M. Purcell, "Effects of Diffusion on Free Precession in Nuclear Magnetic Resonance Experiments," *Phys. Rev.*, vol. 94, no. 3, pp. 630-638, May 1954.
- [5] W. S. Price, "Pulsed-field gradient nuclear magnetic resonance as a tool for studying translational diffusion: Part 1. Basic theory," *Concepts Magn. Reson.*, vol. 9, no. 5, pp. 299-336, Jan. 1997.
- [6] T. Schneider, "Spinal cord diffusion imaging: Challenging characterization and prognostic value," Doctoral Thesis, UCL (University College London), 2013.
- [7] Bammer, F. Fazekas, M. Augustin, J. Simbrunner, S. Strasser-Fuchs, T. Seifert, R. Stollberger, and H. P. Hartung, "Diffusion-weighted MR imaging of the spinal cord," *AJNR AmJ Neuroradiol*, vol. 21, no. 3, pp. 587-591, Mar. 2000.
- [8] P. J. Basser, J. Mattiello, and D. LeBihan, "Estimation of the effective self-diffusion tensor from the NMR spin echo," *J Magn Reson B*, vol. 103, no. 3, pp. 247-254, Mar. 1994.
- [9] P. J. Basser and C. Pierpaoli, "Microstructural and physiological features of tissues elucidated by quantitative-diffusion-tensor MRI," *J Magn Reson B*, vol. 111, no. 3, pp. 209-219, Jun. 1996.
- [10] P. B. Kingsley, "Introduction to diffusion tensor imaging mathematics: Part III. Tensor calculation, noise, simulations, and optimization," *Concepts Magn. Reson.*, vol. 28A, no. 2, pp. 155-179, Mar. 2006.
- [11] A. Kumar, D. Welti, and R. R. Ernst, "NMR Fourier zeugmatography. 1975," *J. Magn. Reson.*, vol. 213, no. 2, pp. 495-509, Dec. 2011.
- [12] M. Poustchi-Amin, S. A. Mirowitz, J. J. Brown, R. C. McKinstry, and T. Li, "Principles and applications of echo-planar imaging: a review for the general radiologist," *Radiographics*, vol. 21, no. 3, pp. 767-779, Jun. 2001.

- [13] A. Deshmane, V. Gulani, M. A. Griswold, and N. Seiberlich, "Parallel MR imaging," *J Magn Reson Imaging*, vol. 36, no. 1, pp. 55-72, Jul. 2012.
- [14] R. Brown, Y.-C Cheng, E. Haacke, M. Thompson, e R. Venkatesan, «Sampling and Aliasing in Image Reconstruction», in *Magnetic Resonance Imaging*, John Wiley & Sons Ltd, 2014, pp. 669-700.
- [15] K. P. Pruessmann, M. Weiger, M. B. Scheidegger, and P. Boesiger, "SENSE: sensitivity encoding for fast MRI," *Magn Reson Med*, vol. 42, no. 5, pp. 952-962, Nov. 1999.
- [16] M. A. Griswold, P. M. Jakob, R. M. Heidemann, M. Nittka, V. Jellus, J. Wang, B. Kiefer, and A. Haase, "Generalized autocalibrating partially parallel acquisitions (GRAPPA)," *Magn Reson Med*, vol. 47, no. 6, pp. 1202-1210, Jun. 2002.
- [17] J. Puly, Chapter 2: Partial Fourier Reconstruction, *Lecture Notes* http://users.fmrib.ox.ac.uk/~karla/reading_group/lecture_notes/Recon_Pauly_read.pdf, *Stanford University*, [Available online February 2016].
- [18] X. Liu, "Magnetic Resonance Diffusion Tensor Imaging: Distortion Correction Methods and Their Applications in High-Resolution In vivo Monkey Brain Scans," Doctoral Thesis, University of Rochester, Rochester, New York, 2009.
- [19] P. Jezzard e R. S. Balaban, «Correction for geometric distortion in echo planar images from B0 field variations», *Magn Reson Med*, vol. 34, n. 1, pp. 65-73, Jul. 1995.
- [20] H. Zeng e R. T. Constable, «Image distortion correction in EPI: Comparison of field mapping with point spread function mapping», *Magn. Reson. Med.*, vol. 48, n. 1, pp. 137-146, Jul. 2002.
- [21] Chang H, Fitzpatrick JM. A technique for accurate magnetic resonance imaging in the presence of field inhomogeneities. *IEEE Trans Med Imaging* 1992;11:319-29.
- [22] H. U. Voss, R. Watts, A. M. Uluğ, e D. Ballon, «Fiber tracking in the cervical spine and inferior brain regions with reversed gradient diffusion tensor imaging», *Magn Reson Imaging*, vol. 24, n. 3, pp. 231-239, Abr. 2006.
- [23] D. Weishaupt, V. D. Köchli, and B. Marincek, *How does MRI work?: An Introduction to the Physics and Function of Magnetic Resonance Imaging*. Springer Science & Business Media, 2008.
- [24] E. U. Saritas, S. J. Holdsworth, and R. Bammer, "Chapter 2.3 - Susceptibility Artifacts," in *Quantitative MRI of the Spinal Cord*, J. C.-A. A. M. Wheeler-Kingshott, Ed. San Diego: Academic Press, 2014, pp. 91-105.
- [25] J. B. Andre and R. Bammer, "Advanced Diffusion-Weighted Magnetic Resonance Imaging Techniques of the Human Spinal Cord," *Top Magn Reson Imaging*, vol. 21, no. 6, pp. 367-378, Dec. 2010.

- [26] A. W. Anderson and J. C. Gore, "Analysis and correction of motion artifacts in diffusion weighted imaging," *Magn Reson Med*, vol. 32, no. 3, pp. 379–387, Sep. 1994.
- [27] G. Zaharchuk, E. U. Saritas, J. B. Andre, C. T. Chin, J. Rosenberg, T. J. Brosnan, A. Shankaranarayanan, D. G. Nishimura, and N. J. Fischbein, "Reduced field-of-view diffusion imaging of the human spinal cord: comparison with conventional single-shot echo-planar imaging," *AJNR Am J Neuroradiol*, vol. 32, no. 5, pp. 813–820, May 2011.
- [28] E. U. Saritas, C. H. Cunningham, J. H. Lee, E. T. Han, and D. G. Nishimura, "DWI of the spinal cord with reduced FOV single-shot EPI," *Magn Reson Med*, vol. 60, no. 2, pp. 468–473, Aug. 2008.
- [29] C. Beaulieu, "The basis of anisotropic water diffusion in the nervous system - a technical review," *NMR Biomed*, vol. 15, no. 7–8, pp. 435–455, Dec. 2002.
- [30] M. E. Moseley, Y. Cohen, J. Kucharczyk, J. Mintorovitch, H. S. Asgari, M. F. Wendland, J. Tsuruda, and D. Norman, "Diffusion-weighted MR imaging of anisotropic water diffusion in cat central nervous system," *Radiology*, vol. 176, no. 2, pp. 439–445, Aug. 1990.
- [31] B. M. Ellingson, S. N. Kurpad, S.-J. Li, and B. D. Schmit, "In vivo diffusion tensor imaging of the rat spinal cord at 9.4T," *J Magn Reson Imaging*, vol. 27, no. 3, pp. 634–642, Mar. 2008.
- [32] J. C. Ford, D. B. Hackney, D. C. Alsop, H. Jara, P. M. Joseph, C. M. Hand, and P. Black, "MRI characterization of diffusion coefficients in a rat spinal cord injury model," *Magn Reson Med*, vol. 31, no. 5, pp. 488–494, May 1994.
- [33] B. M. Ellingson, S. N. Kurpad, and B. D. Schmit, "Ex vivo diffusion tensor imaging and quantitative tractography of the rat spinal cord during long-term recovery from moderate spinal contusion," *J Magn Reson Imaging*, vol. 28, no. 5, pp. 1068–1079, Nov. 2008.
- [34] C. A. Clark, G. J. Barker, and P. S. Tofts, "Magnetic resonance diffusion imaging of the human cervical spinal cord in vivo," *Magn Reson Med*, vol. 41, no. 6, pp. 1269–1273, Jun. 1999.
- [35] M. Ries, R. A. Jones, V. Dousset, and C. T. Moonen, "Diffusion tensor MRI of the spinal cord," *Magn Reson Med*, vol. 44, no. 6, pp. 884–892, Dec. 2000.
- [36] M. Descoteaux and J. G. Webster, "High Angular Resolution Diffusion Imaging (HARDI)," in *Wiley Encyclopedia of Electrical and Electronics Engineering*, John Wiley & Sons, Inc., 1999.
- [37] D. S. Tuch, "Q-ball imaging," *Magn Reson Med*, vol. 52, no. 6, pp. 1358–1372, Dec. 2004.

- [38] J. Cohen-Adad, M. Descoteaux, S. Rossignol, R. D. Hoge, R. Deriche, and H. Benali, "Detection of multiple pathways in the spinal cord using q-ball imaging," *Neuroimage*, vol. 42, no. 2, pp. 739–749, Aug. 2008.
- [39] B. M. Ellingson, J. L. Ulmer, S. N. Kurpad, and B. D. Schmit, "Diffusion tensor MR imaging of the neurologically intact human spinal cord," *AJNR Am J Neuroradiol*, vol. 29, no. 7, pp. 1279–1284, Aug. 2008.
- [40] D. Facon, A. Ozanne, P. Fillard, J.-F. Lepeintre, C. Tournoux-Facon, and D. Ducreux, "MR diffusion tensor imaging and fiber tracking in spinal cord compression," *AJNR Am J Neuroradiol*, vol. 26, no. 6, pp. 1587–1594, Jul. 2005.
- [41] S. Rajasekaran, R. M. Kanna, R. Karunanithi, and A. P. Shetty, "Diffusion tensor tractography demonstration of partially injured spinal cord tracts in a patient with posttraumatic Brown Sequard syndrome," *J Magn Reson Imaging*, vol. 32, no. 4, pp. 978–981, Oct. 2010.
- [42] D. Ducreux, J.-F. Lepeintre, P. Fillard, C. Loureiro, M. Tadié, and P. Lasjaunias, "MR diffusion tensor imaging and fiber tracking in 5 spinal cord astrocytomas," *AJNR Am J Neuroradiol*, vol. 27, no. 1, pp. 214–216, Jan. 2006.
- [43] D. M. Wingerchuk, C. F. Lucchinetti, and J. H. Noseworthy, "Multiple Sclerosis: Current Pathophysiological Concepts," *Lab Invest*, vol. 81, no. 3, pp. 263–281, Jan. 2001.
- [44] E. Sbardella, F. Tona, N. Petsas, P. Pantano, E. Sbardella, F. Tona, N. Petsas, and P. Pantano, "DTI Measurements in Multiple Sclerosis: Evaluation of Brain Damage and Clinical Implications, DTI Measurements in Multiple Sclerosis: Evaluation of Brain Damage and Clinical Implications," *Multiple Sclerosis International, Multiple Sclerosis International*, vol. 2013, 2013, p. e671730, Mar. 2013.
- [45] F. Fink, J. Klein, M. Lanz, T. Mitrovics, M. Lentschig, H. K. Hahn, and H. Hildebrandt, "Comparison of Diffusion Tensor-Based Tractography and Quantified Brain Atrophy for Analyzing Demyelination and Axonal Loss in MS," *Journal of Neuroimaging*, vol. 20, no. 4, pp. 334–344, Oct. 2010.
- [46] R. Brown, Y.-C Cheng, E. Haacke, M. Thompson, e R. Venkatesan, «Sampling and Aliasing in Image Reconstruction», in *Magnetic Resonance Imaging*, John Wiley & Sons Ltd, 2014, pp. 669–700.
- [47] P. Li, X. Yu, J. Griffin, J. M. Levine, e J. Ji, «High-resolution MRI of spinal cords by compressive sensing parallel imaging», em *2015 37th Annual International Conference of the IEEE Engineering in Medicine and Biology Society (EMBC)*, 2015, pp. 4266–4269.
- [48] Questions and Answers in MRI, <http://mriquestions.com/array-coils.html> [Available Online September 2016].
- [49] R. F. Lee, R. O. Giaquinto, e C. J. Hardy, «Coupling and decoupling theory and its

- application to the MRI phased array», *Magn Reson Med*, vol. 48, n. 1, pp. 203-213, Jul. 2002.
- [50] R. F. Lee, R. O. Giaquinto, e C. J. Hardy, «Coupling and decoupling theory and its application to the MRI phased array», *Magn Reson Med*, vol. 48, n. 1, pp. 203-213, Jul. 2002.
- [51] M. A. Bernstein, K. F. King, e X. J. Zhou, *Handbook of MRI Pulse Sequences*. Elsevier, 2004.
- [52] D. B. Russakoff, C. Tomasi, T. Rohlfing, e C. R. M. Jr, «Image Similarity Using Mutual Information of Regions», in *Computer Vision - ECCV 2004*, T. Pajdla e J. Matas, Eds. Springer Berlin Heidelberg, 2004, pp. 596-607.
- [53] A. Collignon, F. Maes, D. Delaere, D. Vandermeulen, P. Suetens, e G. Marchal, «Automated multi-modality image registration based on information theory», *In: Bizais*, 1995.
- [54] Chang Chia-Hao, “DtiSearch - DTI Fiber Tractography (Streamline Tracking Technique)”, NTHU Magnetic Resonance Imaging Laboratory Department of Biomedical Engineering and Environmental Sciences, 2012 [Available online January 2016].
https://www.mathworks.com/matlabcentral/fileexchange/34008-dti-fiber-tractography--streamline-tracking-technique-/all_files.
- [55] A. Sewonu, “Développements Méthodologiques et Techniques pour le Contrôle Qualité en Imagerie par Résonance Magnétique”, École Doctorale BioSE (Biologie-Santé-Environnement), Doctoral Thesis, Université de Lorraine, 2014. [Available Online September 2016] http://docnum.univ-lorraine.fr/public/DDOC_T_2014_0002_SEWONU.pdf
- [56] M. Bai e S. Luo, «Improved Fiber Tracking for Diffusion Tensor MRI», em *Medical Imaging and Augmented Reality*, G.-Z. Yang e T.-Z. Jiang, Eds. Springer Berlin Heidelberg, 2004, pp. 171-178.
- [57] Inglese M, Bester M. “Diffusion imaging in multiple sclerosis: research and clinical implications”. *NMR in biomedicine*. 2010;23(7):865-872. doi:10.1002/nbm.1515.

TEDI - Tool for EPI Distortion Improvement

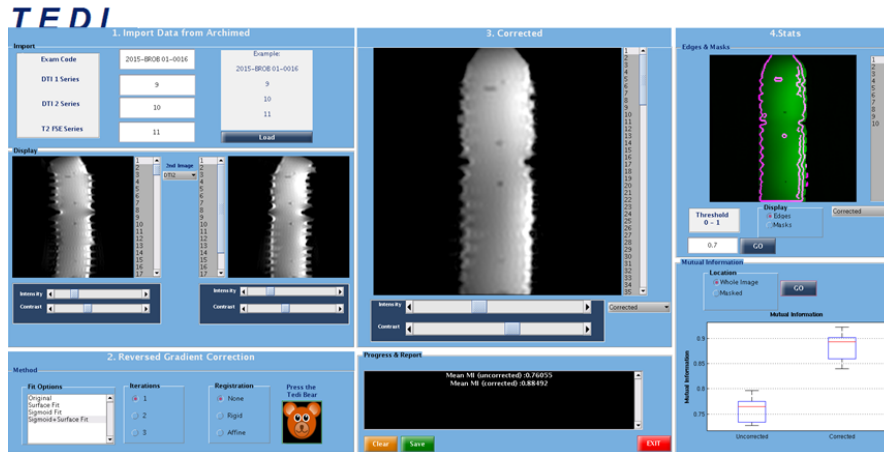
Requirements:

This interface was created using Matlab R2013a (version 8.1) under Linux environment. It is recommended using this or later versions of Matlab. In order to successfully use this interface connection between Matlab and Archimed3 (database for the images) is necessary. Moreover some inhouse Matlab functions in the database are called. Before starting the interface set the path to these functions. <Add to path> → <Select folders and subfolders>. Everything (including the files to run the interface `tedicor.fig` and `tedicor.m`) are in the zipped folder “workspace”:

Summary:

TEDI is a Matlab interface for the correction of EPI distortions in DTI images. The correction methods are based on the reversed gradient method describe in this thesis. For this method to work, two EPI images with opposite phase encoding direction must have been acquired. Theoretically, these two images will have distortions in opposite direction in the PE direction and can be combined to produce the undistorted image. A detailed description of the interface is given in this tutorial. The order of execution of each panel is as follows 1. Import Data from Archimed, 2. Correction, 3. Corrected, 4. Stats.

A figure of the full interface is displayed bellow.



1. Import Images from Archimed

- To start double click on the tedicor.fig file or open the tedicor.m in Matlab and run the code;
- First, specify the exam code and the series of the two DTI datasets and the T2FRFSE dataset (without distortions) for comparison. The images are imported as 3D volumes in “signed 16-bit” format (int16). For the DTI images, the size is (Nx, Ny, Nz), where Nx and Ny are the dimension of the image in pixels and Nz is the number of slices times the number of diffusion directions (including the b0 measurement). For the FRFSE image Nz is the number of slices;
- Then press the Load button to import the images;

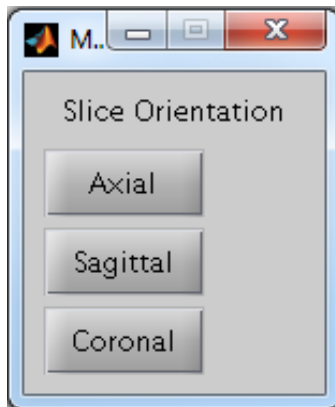
1. Import Data from Archimed

Import

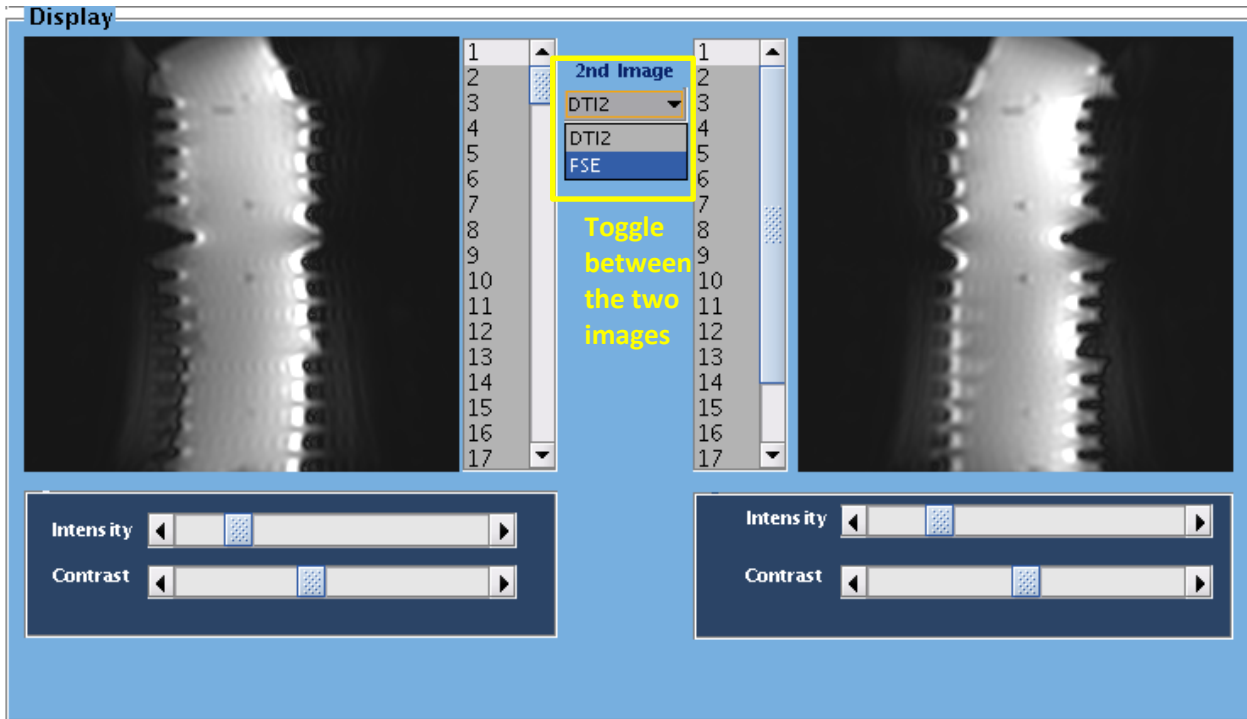
Exam Code	→	2015-BROB 01-0016	Example: 2015-BROB 01-0016 9 10 11
DTI 1 Series	→	9	
DTI 2 Series	→	10	
T2 FSE Series	→	11	

Load

- A window will pop up to specify the slice orientation for this dataset;



- In the left panel, the first DTI dataset is automatically displayed;
- In the right panel toggle between the FRFSE and the second DTI dataset;
- Change contrast and intensity using the sliders to better visualize the images;
- Scroll between different slices (and diffusion directions in the case of the DTI datasets);



2. Reversed Gradient Correction

- Choose the fit options for the calculation of the displacement map for the correction. For more details about each fit option (Original, Surface Fit, Sigmoid Fit, Sigmoid + Surface Fit) read section 2.4.3 of this thesis;
- Choose the number of iterations (1, 2, 3) and registration options (None, Rigid, Affine); 1 Iteration and no registration are recommended.
- Press on the bear logo button to apply correction;

2. Reversed Gradient Correction

Method

Fit Options

- Original
- Surface Fit
- Sigmoid Fit
- Sigmoid+Surface Fit

Iterations

1

2

3


Registration

None

Rigid

Affine

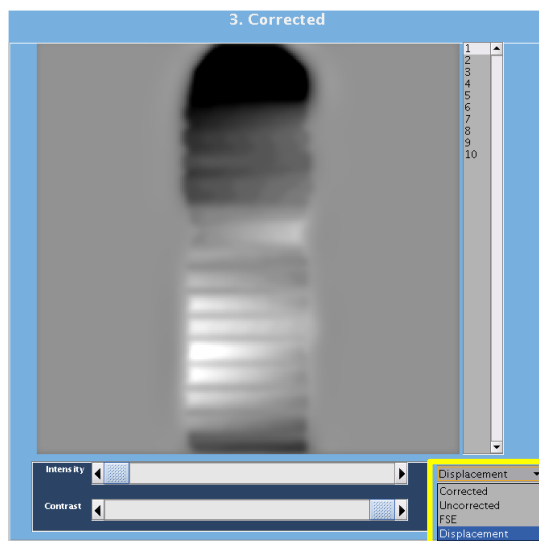
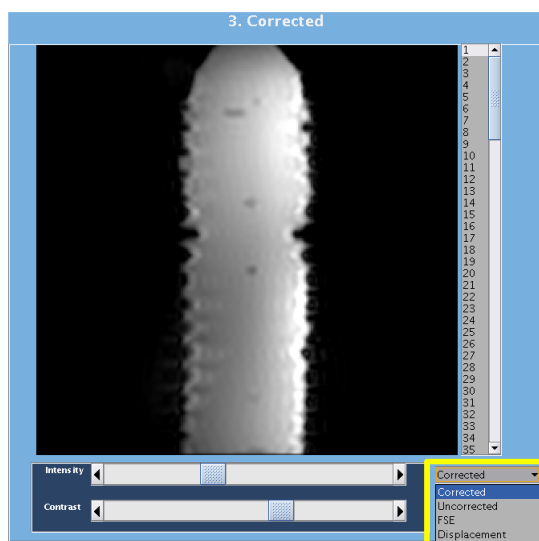
Press the Tedi Bear



Apply correction

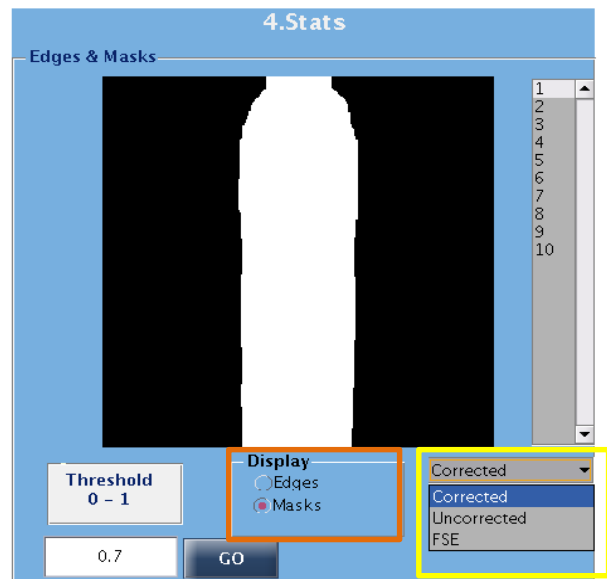
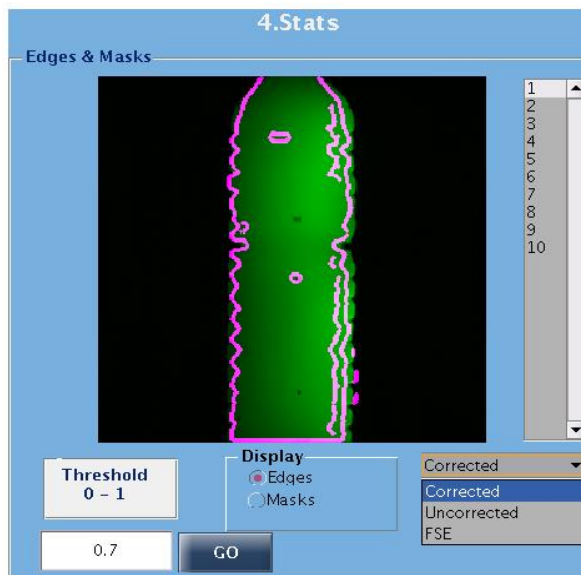
3. Corrected

- This panel displays the results after the correction;
- Toggle between the Corrected, Uncorrected, FRFSE images and the pixel Displacement map;
- Change contrast and intensity using the sliders to better visualize the images;
- Scroll between different slices (and diffusion directions in the case of the DTI dataset);

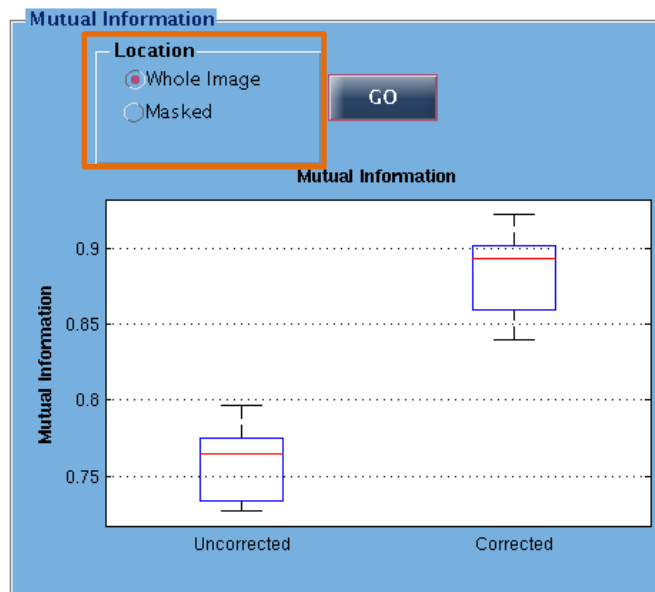


4. Stats

- In the top-right panel compute the masks and edges of the images;
- First define the threshold (between 0 and 1) for the binarization of the images;
- Choose what to display (Masks or Edges);
- Press Go;
- Then simply choose what to display (Masks or Edges) and toggle between Corrected, Uncorrected and FRFSE images;
- When “Edges” are displayed, the contour of the selected image (Corrected, Uncorrected, FRFSE) is shown in magenta over the FRFSE image in green;
- When “Masks” is selected the mask of the selected image is displayed;

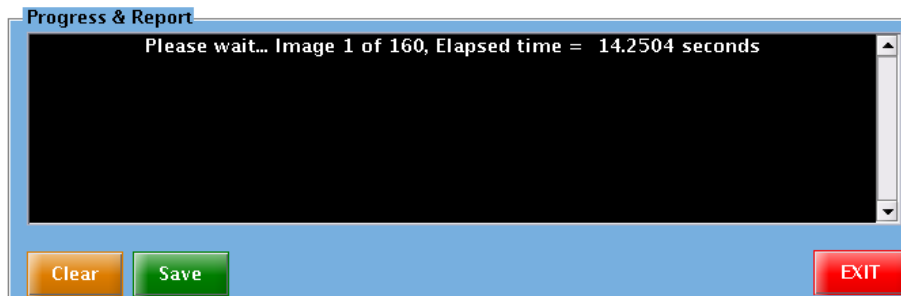


- In the bottom-right panel compute the mutual information. In this case the MI is being calculated between the uncorrected image and the distortion-free FRFSE image and between the corrected image and the distortion-free FRFSE image;
- Choose if the MI is computed in the “Whole Image” or in the “Masked image”;
- Press Go;
- Boxplots are displayed. The values are from all the slice;

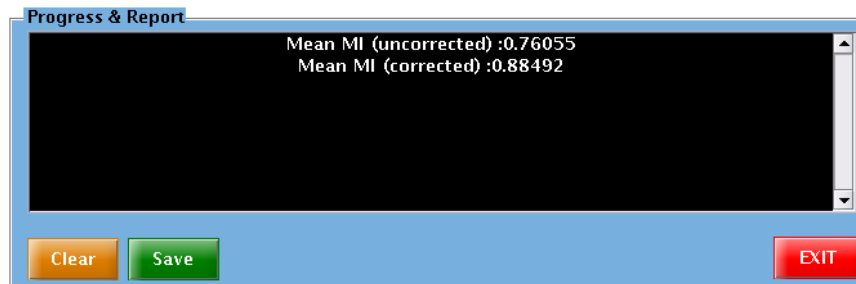


Progress and Report

- Here, error messages and the computation progress are displayed.



- The mean values of the mutual information computed above are also displayed here;



- Press Clear to clean the message board;
- Press Save to save the data in a .mat file; specify a name (e.g. “data”) and a path;
- Press Exit to exit the program;
- After the data is saved it can be loaded it into Matlab workspace;
- The data is saved as a structure and some relevant fields are displayed in the figure below.

Field	Value	Min	Max
logoMap	[]		
output	364.0065	364...	364...
DT11info	<1x1 struct>		
DT12info	<1x1 struct>		
T2info	<1x1 struct>		
DT11_data	<256x256x160 int16>	<To...	<To...
DT12_data	<256x256x20 int16>	<To...	<To...
T2FSE_data	<256x256x10 int16>	<To...	<To...
numberSlices	10	10	10
numberDir	16	16	16
Nz	160	160	160
sliceOr	2	2	2
MaxDT11	32767	32767	32767
Xlim	[0.5000 256.5000]	0.50...	256...
Ylim	[0.5000 256.5000]	0.50...	256...
Nx	256	256	256
Ny	256	256	256
corrected_orig	<256x256x160 single>	<To...	<To...
corrected_sigm	<256x256x160 single>	<To...	<To...
corrected_final	<256x256x160 single>	<To...	<To...
displacement	<256x256x10 double>	<To...	<To...
corrected_surf	<256x256x160 single>	<To...	<To...
corrected_sig...	<256x256x160 single>	<To...	<To...
edgesEPI1	<256x256x10 logical>	<To...	<To...
edgesEPI2	<256x256x10 logical>	<To...	<To...
edgesCORR	<256x256x10 logical>	<To...	<To...
edgesT2	<256x256x10 logical>	<To...	<To...
T2FSE_data2	<256x256x10 int16>	<To...	<To...
maskDT11	<256x256x10 logical>	<To...	<To...
maskDT12	<256x256x10 logical>	<To...	<To...
maskCORR	<256x256x10 logical>	<To...	<To...
maskT2	<256x256x10 logical>	<To...	<To...
fused_corr	<4-D uint8>	<To...	<To...